M 2020

U.PORTO
FEUP FACULDADE DE ENGENHARIA
UNIVERSIDADE DO PORTO

CHARACTERIZATION OF ADVANCED PTL STRUCTURES FOR PEM ELECTROLYZERS AT HIGH TEMPERATURES AND ELEVATED CURRENT DENSITIES

BÁRBARA LOPES COSTA GOMES

DISSERTAÇÃO DE MESTRADO APRESENTADA
À FACULDADE DE ENGENHARIA DA UNIVERSIDADE DO PORTO EM
ENGENHARIA QUÍMICA

Master in Chemical Engineering

Characterization of Advanced PTL Structures for PEM Electrolyzers at High Temperatures and Elevated Current Densities

Master dissertation

of

Bárbara Lopes Costa Gomes

Developed within the course of dissertation

held in

Institute of Engineering Thermodynamics / Department of Electrochemical Energy Technology

Supervisor at FEUP: **Prof. Dr. Adélio Mendes**

Supervisor at DLR: **MSc. Svenja Stiber**

July 2020

Acknowledgments

I would like to firstly and foremost thank DLR and the Institute of Engineering Thermodynamics in the name of Prof. Friedich, for providing me the opportunity to develop my research, for the trust and support that all colleagues places in FEUP students allowing them to live this experience.

A special thank you to my supervisors in DLR, Dr. Aldo Gago and Svenja Stiber, whose knowledge, guidance, time and support were restless, and I will never forget how much I grew and learned in this challenging project thanks to you. Further regards must also be given to Jörg Bürkle and Tobias Morawietz, for their guidance around new materials, testbenches and software and whose video calls challenged all schedules.

To my supervisor at FEUP, Prof. Adélio Mendes, I must thank for the guidance and motivation throughout the semester as well the invested in my work.

It is impossible to fail to recognize how much I have grown and learned throughout my entire academic path, reason why I must thank all my professors in FEUP, with special regards Prof. Miguel Madeira and Prof. Joaquim Faria, for their guidance and inspiration along the years.

I am very grateful for the financial support from ERASMUS+ and all the team behind the programme, to the DCOOP and International Office teams. Thank you for supporting all students in their unforgettable experience abroad.

To all my colleagues from FEUP and student groups I must thank for all the breaks, for all the sweat and tears shared throughout the years, and to all the laughs, all the shared stages, and the inspiration to follow each passion like nothing in the world could stop us. To the relentless Tuna Feminina do Orfeão Universitário do Porto, I will carry with me all the friendships, laughs and late nights.

To my parents, grandparents and godmother, for all the support, sacrifices and guidance, being this a hug, a shared laugh or a big talk: without you I don't know where I'd be.

Professor Adélio Mendes, the university supervisor in this dissertation, is a member of LEPABE – Laboratório de Engenharia de Processos, Ambiente Biotecnologia e Energia, financed by: Financiamento Base - UIDB/00511/2020 da Unidade de Investigação - Laboratório de Engenharia de Processos, Ambiente, Biotecnologia e Energia – LEPABE – financed by national funds through FCT/MCTES (PIDDAC).

Abstract

Even though environmental measures are being taken around the world, the CO2 emissions keep rising and establishing new goals in areas such as energy power supply. This industry searches for technologies that can satisfy all benefits from renewable energy sources as electrolysers. This solution called Power-to-X technology is used to convert electrical energy to chemical energy in form of hydrogen by proton exchange membrane electrolysis (PEMWE). Even though state of the art carries studies using a current density of 2.0 $A \cdot cm^{-2}$, the research for PEM at reduced investment costs focuses now on standards of 4.0 or even 6.0 $A \cdot cm^{-2}$ and the need to improve the efficiency of the cell at these current densities.

In this study it is described the characterization of titanium porous transport layers at 2.0, 4.0 and 6.0 $A \cdot cm^{-2}$, consisted of a mesh structure and a microporous layer. The study on the compression pressure applied at the assembly was done at 0.2 N·m, 0.45 N·m, 1.0 N·m, 2.2 N·m and 3.0 N·m, and it was concluded that the optimum value was 1.0 N·m, since this is the value that offers a higher efficiency and minimizes overpotentials. The limitations dominated by the slow rate of activation of the OER decrease up to 1.0 N·m. Nevertheless, at higher compression pressures the mechanical stress becomes too intense and creates holes in the MEA.

After studies on the physical characterization of coated PTLs, the focus on electrochemical characterization determines how the morphology of these materials performs at elevated temperatures and current densities. As a result, Ti-GKN performed better than other PTLs during the recording of polarization curves, achieving 2.70 V at 4.0 $A \cdot cm^{-2}$. Electrochemical impedance spectroscopy registered the lowest ohmic resistances and mass transportation limitation with Ti-GKN, supporting its ohmic resistance at 159 $m\Omega \cdot cm^2$, while the ohmic resistances of Ti mesh and sintered Ti are approximately 165 $m\Omega \cdot cm^2$ and 182 $m\Omega \cdot cm^2$, respectively. The characterization concludes that a coated PTL has improved mass transport losses at low and high current densities. The Ti-GKN PTL shows optimal electron and mass transport throughout the range of current densities, even though the overpotentials generated at the uncoated PTL prevent an economical cell voltage.

In a parallel study, a simulation work was carried out using SEM images and GeoDict as a material property characterization software. Images of Ti-Ti/Nb, Ti-GKN and Ti mesh were imported and the following properties predicted: bubble point, tortuosity factor and the capillary pressure curve.

Keywords (theme): PEM electrolysis, elevated temperature, elevated current density, cost reduction, gas diffusion, mass transportation.

Resumo

Apesar da contínua implementação de medidas ambientais em todo o mundo, as emissões de CO2 continuam em aumento e introduzindo novas metas em indústrias como o fornecimento de energia. Esse setor procura tecnologias que possam satisfazer todos os benefícios de fontes de energia renováveis, como é o caso dos eletrolisadores. Esta solução denominada também por tecnologia *Power-X* é usada para converter energia elétrica em energia química na forma de hidrogênio, por eletrólise de uma membrana de protões. Embora o estado da arte mencione estudos usando uma intensidade de corrente de 2.0 $A \cdot cm^{-2}$, é notória a necessidade de replicar as eficiências de células em condições de 4.0 e 6.0 $A \cdot cm^{-2}$.

Neste artigo é descrita a caracterização de camadas porosas de transporte de titânio em 2.0, 4.0 e 6.0 $A \cdot cm^{-2}$, sendo esta estrutura constituída por uma malha e uma camada microporosa. O estudo da pressão de compressão aplicada na montagem foi realizado para 0.2 N·m, 0.45 N·m, 1.0N·m, 2.2 N·m e 3.0 N·m, e otimiza o estudo em 1,0 N·m, já que é este o valor que oferece maior eficiência da célula e minimiza as perdas. As limitações dominadas pela lenta taxa de ativação do REA diminuem até 1,0 N·m. No entanto, em pressões de compressão mais altas, o estresse mecânico torna-se intenso e leva a limitações ao nível da membrana.

Após estudos sobre a caracterização física de PTLs revestidos, o foco na caracterização eletroquímica relaciona a morfologia desses materiais com o seu desempenho em condições de temperaturas e densidades de corrente elevadas. Como resultado, o Ti-GKN teve uma eficiência mais elevada do que outros PTLs durante o registro das curvas de polarização, alcançando 2.70 V a 4.0 $A \cdot cm^{-2}$. A espectroscopia eletroquímica de impedância registrou as menores resistências ohmicas e limitações de transporte de massa com o Ti-GKN, suportando sua resistência ohmica em 159 $m\Omega \cdot cm^2$, enquanto as resistências ômicas do Ti sem revestimento e sinterizado são aproximadamente 165 $m\Omega \cdot cm^2$ e 182 $m\Omega \cdot cm^2$, respectivamente. A caracterização conclui que um PTL revestido minimizou as perdas de transporte de massa em baixas e altas densidades de corrente. O Ti-GKN PTL mostra o transporte ideal de eletrões e de massa em toda a faixa de densidades de corrente.

Num estudo paralelo, foram concluídas simulações usando imagens SEM e o programa GeoDict para caracterização de materiais. As imagens de Ti / Ti-Nb, Ti-GKN e Ti-Ti permitiram prever a analisar as seguintes propriedades: ponto de bolha, fator de tortuosidade e curva de pressão capilar.

Palavras-passe (tema): PEM eletrólise, temperatura elevada, densidade de corrente elevada, redução de custos, difusão gasosa, transporte de massa.

Declaration

I hereby declare, under word of honour, that this work is original and that all non-original contributions is indicated, and due reference is given to the author and source

Bárbara Lopes Costa Gomes

05-07-2020

Index

1 Introduction 1
1.1 Framing and Presentation of the Work 1
1.2 Presentation of DLR 3
1.3 Contribution of the Author to the Work 4
1.4 Organization of the Thesis 4
2 Context and State of the Art 7
2.1 Fundamentals of PEM Electrolysis 7
2.1.1 Thermodynamics 8
2.1.2 Overpotentials of PEM electrolyzers 10
2.2 PEM Electrolyzer's Main Components 11
2.2.1 Bipolar Plates (BPPs) 11
2.2.2 Membrane Electrode Assembly (MEA) 12
2.2.3 Porous Transport Layer (PTL) 13
2.3 PEM Electrolyzer's System Overview 14
3 Materials and Methods 17
3.1 Materials and Equipment 18
3.2 PTL Manufacturing (Coating Methods) 18
3.2.1 Vacuum Plasma Spraying (VPS) 19
3.2.2 Powder Metallurgy (PM) 19
3.3 PEM Electrolyzer Assembly and Test Bench 20
3.4 Scanning Electron Microscopy (SEM) 22
3.5 Physical Characterization 23
3.5.1 ICR Measurements 23
3.6 Electrochemical Characterization 23
3.6.1 Polarization Curve 23
3.6.2 EIS 25
3.7 GeoDict Simulation 27

4 Results and Discussion 31
4.1 Evaluation of the Characterization with Different Compression Pressures..... 31
4.2 Evaluation of the Physical Characterization (ICR Measurements) 34
4.3 Evaluation of the Electrochemical Characterization 36
4.4 GeoDict Simulation Results..... 39
4.5 Availability for Grid Services 40
5 Conclusion..... 43
6 Assessment of the work done 45
6.1 Objectives Achieved..... 45
6.2 Final Assessment 45
7 References 47
Appendice A – Polarization Curves of Ti-GKN and Ti mesh at Different Compression Pressures 53
Appendice B – GeoDict Simulation Full Results 54

List of Figures

Figure 2.1 - Schematic of a PEM cell. *8*

Figure 2.2 - Relation between the activation energy (E_a) and the reaction progress over time in an endothermic reaction (extracted from [25]). *10*

Figure 2.3 - Representation of a flow diagram of a PEM electrolyzer system [34]. *14*

Figure 2.4 - Examples on materials for the anode PTL in a PEM electrolyzer: a) discs, b) sintered titanium, c) titanium felt, d) carbon, e) mesh (extracted from [28]). *15*

Figure 3.1 - Timeline and phases of the electrochemical characterization of the PTLs in the PEM electrolyzer cells. *17*

Figure 3.2 - Technique of VPS (extracted from [26]). *19*

Figure 3.3 - Cell components and structure of a PEM assembly. *21*

Figure 3.4 - SEM images of the Ti mesh (on the left) and Ti-GKN (on the right) PTLs. *22*

Figure 3.5 - Polarization curve (extracted from [26]). *24*

Figure 3.6 - EIS example measurement in a Nyquist diagram. *25*

Figure 3.7 – Exemplary electrical equivalent circuit diagram of the system. *26*

Figure 3.8 - µCT images of samples from: a) Ti-Ti; b) the Ti-Ti/Nb coated PTLs. *28*

Figure 3.9 – a) Import screenshot of GeoDict structure; b) 3D representation of the import. *28*

Figure 4.1 - Pressure foil images at the different compression pressures with cell assemblies using Ti substrate as the PTL. *31*

Figure 4.2 - Polarization curves of the different cell assemblies for multiple compression pressures up to 4 $A \cdot cm^{-2}$ at 90 ºC. *32*

Figure 4.3 - Cell performances at different compression pressures and a current density of 2.0 $A \cdot cm^{-2}$. *32*

Figure 4.4 - Nyquist plots from the EIS measurements at 0.25 $A \cdot cm^{-2}$ with an amplitude of 100 mA and a frequency range from 100 kHz to 50 mHz. *33*

Figure 4.5 - Nyquist plots from the EIS measurements at 2.0 $A \cdot cm^{-2}$ with an amplitude of 200 mA and a frequency range from 100 kHz to 50 mHz. *34*

Figure 4.6 - ICR measurements for the SS-mesh, Ti mesh, sintered Ti and Ti-GKN PTLs. *35*

Figure 4.7 - ICR measurements for the SS-mesh, Ti mesh, sintered Ti and Ti-GKN PTLs for 147.1 $N.cm^{-2}$. *35*

Figure 4.8 - Polarization curves of the different cell assemblies up to 2 $A \cdot cm^{-2}$ at 90 ºC. *36*

Figure 4.9 - Polarization curves of the different cell assemblies up to 6.0 $A \cdot cm^{-2}$ at 90 ºC. *37*

Figure 4.10 - Nyquist plots from the EIS measurements at 0.25 A·cm^{-2} with an amplitude of 100 mA and frequencies from 100 kHz to 100 mHz. 37

Figure 4.11 - Nyquist plots from the EIS measurements at 4.0 A·cm^{-2} with an amplitude of 500 mA and from frequencies 100 kHz to 50 mHz. 38

Figure 4.12 - Capillary pressure curve of the Ti-Ti/Nb and Ti-GKN PTLs..... 39

Figure 4.13 – Grid services protocol (response, phases and parameters). 41

Figure 4.14 – Grid services protocol response at 4.0 A·cm^{-2}..... 41

Figure 4.15 - Polarization curves of Ti-GKN up to 4.0 A·cm^{-2} at 65 ºC before and after the protocol.. 41

Figure 4.16 - Nyquist plots from the EIS measurements of Ti-GKN up to 4.0 A·cm^{-2} with a frequency range from 100 kHz to 50 mHz at 65 ºC before and after the protocol. 42

Figure A.1 - Polarization curves of Ti-GKN for multiple compression pressures up to 4.0 A·cm^{-2}..... 53

Figure A.2 - Polarization curves of Ti mesh for multiple compression pressures up to 4.0 A·cm^{-2}..... 53

Figure B.1 - Capillary pressure curve of the Ti-Ti/Nb, Ti-Ti and Ti-GKN PTLs. 54

List of Tables

Table 1.1 - Comparison of selected hydrogen production methods (extracted from [12]). 2

Table 3.1 - Cell configurations according to its corresponding work plan phase..... 21

Table 4.1 - Bubble point and tortuosity factor of the Ti-Ti/Nb and Ti-GKN PTLs. 39

Table B.1 - Bubble point and tortuosity factor of the Ti-Ti/Nb, Ti-Ti and Ti-GKN PTLs..... 54

Notation and Glossary

a	concentration activity	
E	electrode potential	V
E	efficiency	V
F	faraday constant	96485 $C \cdot mol^{-1}$
G	Gibbs free energy	$J \cdot mol^{-1}$ or $J \cdot kg^{-1}$
H	enthalpy	$J \cdot mol^{-1}$ or $J \cdot kg^{-1}$
i	current	A
j	current density	$A \cdot cm^{-2}$
n	number of moles of electrons transferred	mol
z	number of electrons transferred	
R	universal gas constant	$J \cdot mol^{-1} \cdot K^{-1}$
R	resistance	Ω
S	entropy	$J \cdot K^{-1}$
U	reversible cell voltage	V
T	temperature	K or ºC
Z	impedance	Ω

Greek Letters

Δ	difference operator	
Ɛ	efficiency	%
η	overpotential	V
φ	phase angle	º

Indexes

‘	real
‘’	imaginary
0	standard conditions (25 ºC, 1 atm)
a	activation
bub	bubbles
dif	diffusion
g	gas
l	liquid
ohm	ohmic
th	thermoneutral
r	reactants

List of Acronyms

AC	Alternating current
AST	Accelerated stress test
BPP	Bipolar plate
CAPEX	Capital expenditure
CCM	Catalyst coated membrane
Ch	Characterization
CPE	Constant phase element
DI	Deionized water
DLR	Deutsches Zentrum für Luft- und Raumfahrt
EDX	Energy dispersive X-ray spectroscopy
EIS	Electrochemical impedance spectroscopy
EU	European Union
GDE	Gas diffusion electrode
GDL	Gas diffusion layer
GHG	Greenhouse-gas
HER	Hydrogen evolution reaction
HHV	High heating value
ICP-MS	Inductively coupled plasma mass spectrometry
ICR	Interfacial contact resistance
KPI	Key performance indicator
LTM	Long-term measurement
MEA	Membrane electrode assembly
MPL	Macro-porous layer
MTL	Mass transport limitation
OER	Oxygen evolution reaction
PC	Pre-characterization
PEM	Proton exchange membrane
PFSA	Perfluorsulfonic acid
PM	Powder metallurgy
PTFE	Polytetrafluoroethylene
PTL	Porous transport layers
SEM	Scanning electron microscopy
SS	Stainless steel
VPS	Vacuum Plasma Spraying
XPS	X-ray photoelectron spectroscopy

1 Introduction

1.1 Framing and Presentation of the Work

In the growing topic of key technologies for integrating the increasing share of renewable power through the production of hydrogen, the studies of proton exchange membrane (PEM) water electrolysis technologies are common due to their high operational and capital costs [1]. It is important to understand how this technology fits in the energy demand and supply chain and consequently help to reduce emission for the 1.5°C goal set in 2019 in Madrid by the climate action agreement [2].

According to the United Nations Framework Convention on Climate Change, the framing of new environmental goals is focused on decreasing GHG emissions 30 % compared to 1990 by 2030 [2, 3]. In the European Union (EU), in 2017, renewable energy sources were responsible for only 13.5 % of the total greenhouse gas (GHG) emissions, being the highest contributor the energy industry sector with 77.9 % [4, 5]. In the same year, Portugal takes upon 1.6 % of the total GHG emissions in the EU which translates into a 7 % increase compared to the previous year and 19.4 % compared to 1990 [5, 6].

Despite the demand of energy supply being almost constant, there is a discrepancy between the renewable energy available and the actual demand, leading the introduction of fuel cell and hydrogen technologies. These can lead to an increase in energy efficiency and decentralize production of energy out of fuel sources, consequently reducing GHG emissions [7, 8].

On one hand, hydrogen is produced by energy inputs such as steam reforming natural gas from fossil fuels like propane, synthesis gases such as methanol, partial oxidation of hydrocarbons, and coal gasification, being that these conventional sources represent 96 % of the world's hydrogen production and 70 % of the amount of worldwide electricity generated [7, 9]. On the other hand, hydrogen can be provided by a renewable energy source through water electrolysis, taking its power source from excessive wind or solar energy [10].

Steam methane reforming (SMR) is the most common method of hydrogen production despite of being responsible for the emission of large quantities of CO_2 into the atmosphere. In a similar way, methods provided by fossil fuels carry out as disadvantage the emission of other gases [7, 9]. Nevertheless, these are the methods with the highest cost-efficiency.

In contrast to the other methods, water electrolysis from renewable energies is expected to reach 22 % of hydrogen production by 2050, even though its share is currently at 4 % [4]. This method is the most environmentally friendly approach [7] and the focus of this work. The

market for this technology is growing in expansion and competitiveness as the method that produces high-purity hydrogen of 5.0 quality. This is one of the greatest advantages of this technology, when compared to other electrolysis. Other benefits include short response time, wide operation range, flexibility and low footprint [1, 11]. Table 1.1 compares hydrogen production methods, introducing properties that define them.

Table 1.1 - Comparison of selected hydrogen production methods (adapted from [12]).

Hydrogen production method		GWP	Cost	Energy efficiency
Fossil fuel	Natural gas steam reforming	2.94	8.35	3.75
	Coal gasification with CCS	0	8.02	3.50
Renewable energy	Solar based electrolysis	8.53	0	0.50
	Wind based electrolysis	9.43	1.98	3.10
	Biomass gasification	8.24	8.46	6.50
Ideal (0 emissions, 0 cost, 100% efficiency)		10	10	10

Hydrogen becomes a vector in storage, transportation and use of energy by storing energy that can be restored as electricity. This connection means that hydrogen production processes affect electricity prices [13]. This is one of the obstacles expanding water electrolysis as a main supply of hydrogen as it is more expensive than other methods. The main water electrolysis technologies are alkaline, solid oxide (SOEC) and proton exchange membrane (PEM). They differ mostly in their electrolyte and operation conditions [1]. Even so, PEM electrolysis is the most reliable process for the transport sector due to producing high-purity hydrogen.

Nevertheless, a PEM water electrolyzer can provide both primary and secondary power reserves management, which simplifies a major restrain in electricity grids. This technology implements the concept of “hydrogen economy” which relies on a two-step reversible process: the water dissociation for energy storage and the hydrogen electrochemical combustion in oxygen or air for re-electrification [1, 14]. The energy demand implies, however, flexibility and reactivity of PEM water electrolysis cells in conditions of elevated temperature and high current densities. The major benefits of this technology derive from its compacted structure, making the electrolyte easy to manage as a form of a solid membrane and eliminating time and costs related to post-cleaning. These, however, are balanced by the high investment costs [15].

In fact, the research conducted on increasing performance while reducing related costs reveal that product development is the greatest challenge due to the PEM electrolyzers’

components: bipolar plates (BPPs), porous transport layer (PTL), which account for 43 % of the costs [15], and membrane electrode assembly (MEA). Furthermore, the use of titanium materials is advised due to the material's conductivity and its corrosion resistance, but its price is unattractive in a market perspective [16]. The combat in cost reduction is sustained by two strategies. Firstly, by material substitution of high cost Ti with low-cost material like stainless steel with coating [16]. This, however, inserts as a research topic the development of materials that meet the high-quality H_2 production through high porosity, low contact resistance and high durability with low production costs [17, 18]. Secondly, by changing or optimizing operational conditions that support the necessary efficiency of the cell with a lower active area. To increase the economic attractiveness of PEM electrolysis, the standardized current density must be increased from 2.0 $A \cdot cm^{-2}$ to 4.0 $A \cdot cm^{-2}$, empowering the Power-to-X technology to higher production rate.

Despite of being a common subject of recent studies, a PEM electrolyzer has its performance registered in current densities up to 2.0 $A \cdot cm^{-2}$ at 65 °C, default in replicating cell performances at higher temperatures and current densities with materials that can decrease investment costs and optimize operational conditions, introducing larger capacities to the PEM technology.

This dissertation portraits work focused on the characterization of coated porous transport layers in a 4 cm^2 PEM electrolyzer cell at current densities up to 6.0 $A \cdot cm^{-2}$ at 90 °C, establishing possible new standard materials and operational conditions.

1.2 Presentation of DLR

The German Aerospace Center (Deutsches Zentrum für Luft- und Raumfahrt; DLR) is the national aeronautics and space research center of the Federal Republic of Germany. Its many institutes and facilities offer a wide range of research areas such as aeronautics, space, energy, transport, flow dynamics, security and digitalization. Even though its main focus relays on the research provided by its workers and interns, DLR also provides consultary to customers and project partners, and it's responsible for the planning and implementation of Germany's space activities on behalf of the federal government.

The DLR Institute of Engineering Thermodynamics has departments in Cologne, Ulm, Hamburg and Stuttgart that work together on efficient energy storage systems and energy conversion technologies. Within this institute, the electrochemical energy technology group works on energy-efficient electrochemical converters such as batteries, fuel cells and electrolyzers, being these last ones the focus on the work presented in this thesis. The group continuously puts its focus on stationary energy supply and electromobility, being this done through cell

design, manufacturing or diagnostic processes to system optimization and demonstration, which can be experimental or theoretical studies.

1.3 Contribution of the Author to the Work

The reported research contributes to deepening the understanding of the effect of the performance of an electrolyzer cell using a macro-porous layer coated at the gas diffusion layer at elevated temperature and current density. The author is responsible for the electrochemical characterization of stainless steel and titanium gas diffusion layers, coated by Vacuum Plasma Spraying (VPS) with niobium and/or titanium and by powder metallurgy (PM) with the manufactured material GKN. The author demonstrated results that contribute to new data to PEM electrolysis, behaviour in mass transport resistance, performance and use for grid services.

The author was also responsible for electrochemical measurements by performing polarization curves and electrochemical impedance spectroscopy (EIS) measurements and choosing the most adequate impedance parameters in the impedance device. The electrochemical results and the performance of the electrolyzer were analysed by the author. In addition, physical characterization in regards to interfacial contact resistance measurements (ICR) was done.

Regarding the test bench, the author used a power supply without a remote sensor to introduce a hydraulic compression cell, on which it was not possible to test its electrochemical characterization. In a performance comparison, it was initialized a service grid protocol to validate the requirements of the best performing PTL.

Finally, it was possible to run a simulation program to predict parameters such as the bubble point, the tortuosity factor and the saturation curve from SEM images of PTLs. All scanning electron microscopy and energy dispersive X-ray images were performed by colleagues by colleagues at DLR Institute of Networked Energy Systems in Oldenburg. The access to GeoDict was enabled by a partnership with the University of Esslingen. This study is explained as an addition to the characterizations described on this paper in Chapter 6.

1.4 Organization of the Thesis

After the framework explored within PEMWE technologies, the next chapter explains its context in the market, as well its problematics and the reason for advanced characterization in higher current densities and how this can be applied in recent technologies as a crucial indicator of limiting factor in cell efficiency.

Furthermore, a description of the tests and necessary equipment for ICR measurements, polarization curve and impedance spectroscopy is presented in Materials and Methods as an introduction chapter for Results and Discussion, where the focus relies on the comparison of sample measurements and discussion of cell performance and efficiency.

Finally, followed by the summary of the end results of the characterization of PEMWE cells and a brief description of its advantages within the framed work, chapter 6 proposes new developments or enhancements that can be considered regarding the assessment of the results previously described.

2 Context and State of the Art

In this second chapter there is a focus on the theory behind the research that this work presents. In this context, the framing of electrochemical principles and PEM electrolysis are done, as well as it is explained the technologies used along this work. Being possible that the operational costs are reduced by the use of PEMWE by its possibility of operating at current densities higher than 2.0 $A \cdot cm^{-2}$ [1], it is undeniable that characterization on these cell at higher current densities must be a focus on the research developed on these cells, as the best performance is yet to be found.

2.1 Fundamentals of PEM Electrolysis

One of the best-known energy production methods is known as water electrolysis, characterized by the possibility of converting electrical energy into chemical energy in the form of gases. Water is broken down by a redox reaction using an external power source according to the following reaction equation:

$$2\,H_2O\,(l) \leftrightharpoons 2\,H_2\,(g) + O_2\,(g) \tag{2.1}$$

The reaction enthalpy, denoted as ΔH, represents the amount of energy required to break the water chemical bounds, as a sum of the reaction of water splitting and hydrogen reduction.

A PEM electrolyser presents itself as a unique tool capable of storing energy through the production of hydrogen [1]. Through water electrolysis, it is possible to produce high-quality hydrogen, which allows better efficiency than other means of energy input such as steaming of fossil fuels. This makes electrolysis a renewable energy source that can be developed as an energy storage system and replace other energy resources, therefore embracing discussions around renewable sources for electricity.

A PEMWE has as solid electrolyte a proton exchange or polymer electrolyte membrane that enables high proton conductivity. Its compact design is possible due to the thickness of its materials and it can operate at high-pressure conditions that can go up to 350 bar. [1] A schematic of a PEM cell can be found in Figure 2.1 [9], where the membrane is both an electrolyte and a separator between the half cells.

The water is fed through the anode chamber. Protons migrate due to the influence of an electric field generated by the oxygen on the cathode side to the anode side, where they are reduced, forming hydrogen. The mass transport is supported by the semipermeable

membrane by means of the structure diffusion mechanism. This transfer mechanism enables the protons to be transported through the transfer of charge and not with a aqueous solution.

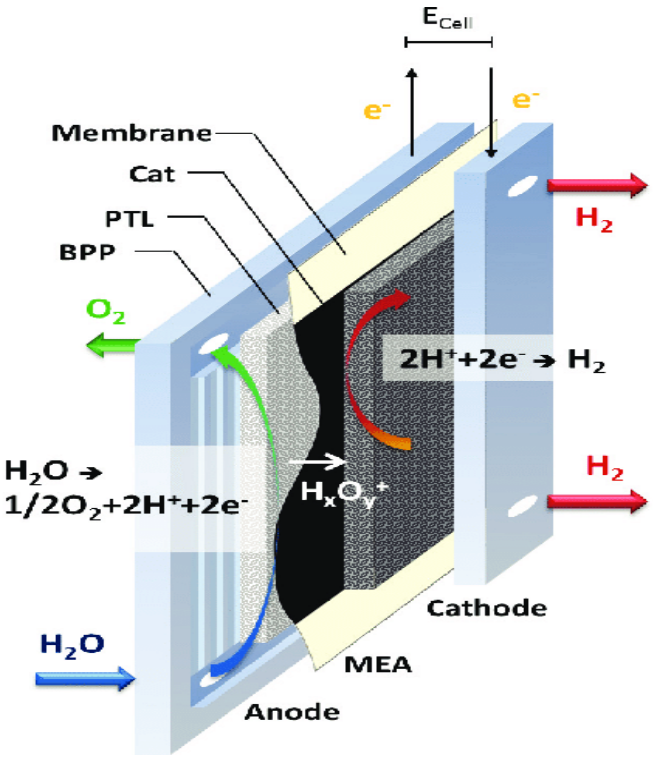

Figure 2.1 - Schematic of a PEM cell.

The overall reaction is an endothermic reaction with a standard enthalpy of reaction of ΔH_0 = 285.83 kJ/mol, represented by the equations below.

$$\text{Anode: } 2\,H_2O\,(l) \leftrightharpoons 4\,H^+\,(aq) + O_2\,(g) + 4\,e^- \tag{2.2}$$

$$\text{Cathode: } 4\,H^+\,(aq) + 4\,e^- \leftrightharpoons 2\,H_2 \tag{2.3}$$

The electrochemical cell is divided in two half-cells, separated by a PEM. Each half-cell consists in a bipolar plate (BPP), a porous transport layer (PTL) as the gas diffusion layer (GDL), and an electrode. So that these are cost- effective, there must be a balance between the production of the PEM electrolyzer and the efficiency of the cell. This balance is a topic on research that focuses mainly on the catalyst for cell and stack assembly for higher efficiencies [21] and adsorption materials and gas separation membranes for the purification of hydrogen [22]. The search to optimize these parameters lacks on answering questions about durability, degradation and availability of precious metals used for the catalysts [23].

2.1.1 Thermodynamics

The thermal properties of the PEM electrolysis cells change along the chemical reaction under standard conditions with all the system environment.

The study of these properties is focused on the standard enthalpy of reaction, ΔH, which can be calculated according to the equation 2.4.

$$\Delta H = \Delta G + T \times \Delta S \tag{2.4}$$

In the electrodes, the reversible half-cell reactions create potential differences that are determined by the difference between the electrode potential electrode and the electrolyte potential electrolyte as in the equation 2.5.

$$\Delta\phi_0 = \phi_{\text{electrode},0} - \phi_{\text{electrolyte},0} \tag{2.5}$$

The potential difference between the cathode and the anode is the reversible cell potential, E, or reversible cell voltage, U_0, and it represents the minimum electrical work required for electrolysis to occur. This property can is determined according to the equation 2.6.

$$U_0 = -\mathrm{E}_0 = \phi_{\text{anode},0} - \phi_{\text{cathode},0} = \frac{\Delta G_0}{z \times \mathrm{F}} \approx 1.23\ \mathrm{V} \tag{2.6}$$

, being z the number of electrons transferred and F the Faraday constant. In this case, z the value is 4, since two electrons are transferred to split per water molecule. The result is a reversible cell voltage of 1.23 V, value of the theoretical decomposition voltage of water at 25°C and without external current flow, since this value is altered according to the temperature and activity of the reactants as demonstrated by the Nernst equation:

$$U_0 = \frac{\Delta G_0}{z \times \mathrm{F}} + \frac{R \times T}{z \times \mathrm{F}} \times \ln\left(\frac{a(\mathrm{H_2O})^2}{a(\mathrm{H_2})^2 \times a(\mathrm{O_2})}\right) \tag{2.7}$$

The equation 2.7 is described for a process at constant temperature with a PEM electrolyzer. Nevertheless, it is possible that the theoretical cell voltage improves at higher temperatures, as long as the entropy is also increased. This favours the study of cell performance at elevated temperatures for the analysis of the PEM limitations in such operating conditions.

On another focus, the theoretical decomposition voltage depends only on the theoretical useful energy. Even so, the necessary activation energy for the water molecules to rise at a higher energy level is compensated by the electrical energy that is not converted into work energy and balances the voltage of 1.23V. This additional calculation with the entropic component is represented on the equation 2.8.

$$U_{0,th} = \frac{\Delta G_0}{z \times \mathrm{F}} + \frac{\Delta S_0 \times T}{z \times \mathrm{F}} = \frac{\Delta H_0}{z \times \mathrm{F}} \tag{2.8}$$

For the same values and in this case, the thermoneutral voltage is approximately 1.48 V. This is the energy registered as heat from the electrolysis, that includes the reaction enthalpy and the minimal electrical energy. According to research in water electrolysis, the increasing number of particles in the gas phase from 0 mol to 3 mol encourages the increase of the

entropy which therefore gets the cell to cool down. This does not happen, however, since the heat generated in the system is released into its environment [22].

2.1.2 Overpotentials of PEM electrolyzers

Like any chemical process, the efficiency of this technology also relies on its losses. Different resistances in the system can lead to deviations in the voltage measurements from the reversible cell voltage by inhibiting the kinetic processes of the electrode reaction. In the case of PEM electrolysis, the kinetic losses responsible for the decrease of the real potential are governed by the following [24]: ohmic losses (η_{ohm}); activation losses (η_a), due to the electrochemical reactions at the anode and cathode [25]; and mass transport losses.

The ohmic losses derive from the flow of electrons through the porous transport layers (PTL) and electrodes, that is, the internal resistance of the cell system, and to the conduction of protons through the PEM [25] and increase along with the temperature and current density [24]. The ohmic overpotentials are determined by the equation 2.9.

$$\eta_{ohm} = \mathrm{I} \times \sum_{\mathrm{i}} \mathrm{R_i} \tag{2.9}$$

On another perspective, and given that the activation energy, E_a, is the minimum amount of energy to apply for the electrochemical reaction to initiate, the use of catalysts on a reaction reduces its activation energy, since it lowers the energy level of the activated complex, reducing the internal energy and therefore increasing the reaction kinetics [26].

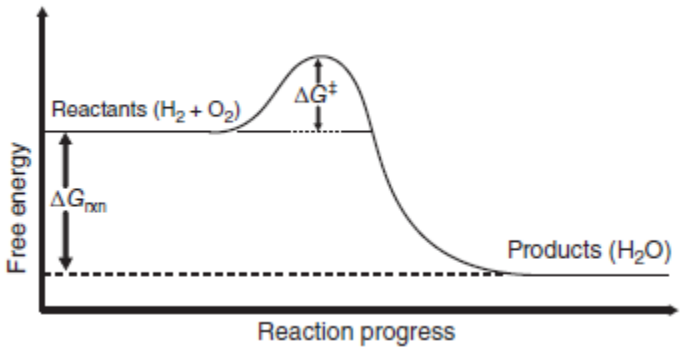

Figure 2.2 - Relation between the activation energy (Ea) and the reaction progress over time in an endothermic reaction (extracted from [26]).

Figure 2.2 shows how the activation energy can be affected using a catalyst through the reaction history during the electrolysis process, given that it is an endothermic reaction. The loss of activation is calculated by the equation 2.10. A higher resistance translates into the electron transfer requiring additional energy so that the electrons can pass through the transport layer.

$$\eta_{\mathrm{a}} = \frac{\mathrm{R} \times T}{z \times \mathrm{F}} \times \ln\left(\frac{i}{i_0}\right) \tag{2.10}$$

where i is the current of operating conditions and i_0 the one from the reference state.

The mass transport overpotentials are a direct result of the morphology of the components BPP and PTL, blockage of pores in the PTL from the gas bubbles (η_{bub}), diffusion and convection mechanisms (η_{diff}) [25], and therefore increase along with the current density. The resulting overpotentials at current densities higher than 1.5 A·cm^{-2} can therefore be explained by excessive reaction speed when compared to the speed of gas removal since the gas molecules occupy the active centers of the catalysts and the reaction cannot take place. The overpotential is calculated using equation 2.11.

$$\eta_{\mathrm{a}} = \frac{\mathrm{R} \times \mathrm{T}}{\mathrm{z} \times \mathrm{F}} \times \ln\left(\frac{\mathrm{c}}{\mathrm{c}_0}\right) \tag{2.11}$$

, where c_0 corresponds to the concentration of oxygen in the gas-water mixture on the active surface of the electrode and c_0 describes a chosen reference state.

The sum of all these losses, adding the reversible cell potential, *E*, results on the real cell potential, E_{cell}, as indicated by the equation 2.12. The kinetic control dominates overpotentials in current densities up to 0.3 A·cm^{-2}, while between 0.3 and 1.5 A·cm^{-2} the losses are measured upon the cell electric control.

$$E_{\mathrm{cell}} = E + \eta_{\mathrm{ohm}} + \eta_{\mathrm{a}} + \eta_{\mathrm{bub}} + \eta_{\mathrm{diff}} \tag{2.12}$$

2.2 PEM Electrolyzer's Main Components

As the major components of a PEM electrolysis cell, it is important to further understand the bipolar plates (BPPs), the membrane electrode assembly (MEA) and the porous transport layer (PTL).

2.2.1 Bipolar Plates (BPP)

The different approaches on the use of a PEM electrolyzer are defined by the bipolar plates (BPPs), since this component is built with or without a flow field integrated on its surface. This flow field allows mass transportation of the resulting gases of the reaction from the electrodes and as the input channel for water for the PTL and, then, to the electrode, where the reaction takes place [19]. In case the BPPs don't have a flow field, this function needs to be provided by the PTL.

The plates are always introduced on the same side of the assembly, as to be attentive to their cleaning. On one hand, the anode side often shows corrosion from the reaction and needs to be sanded, which means that the BPP on the anode side should withstand against the oxidative environment. On the other hand, the BPP on the cathode side must resist hydrogen embrittlement and oxidation at high pressures. The material chosen for the BPPs is dependent not only on the PTL, but also on its stable mechanical integrity [27] as well as good electrical and thermal conductivity [28].

The most desired material for a BPP is titanium due to its stability in corrosive environments. It is, however, the material with an increased ICR due to formed oxide layers [29]. Even though it is possible to decrease the effect, other aspects such as its hardness make alternatives like stainless steel an attractive material [28, 17]. This is, in fact, another parameter on the choice of the material of the BPPs: how cost-effective it is. Even though stainless steel is cheaper and easier to manage than titanium, it realizes metal ions like Cr that can poison the MEA. This can be prevented by coating the plates with titanium, preventing poisoning of other components and corrosion [29], and allowing this material to be used in BPP on the anode side. Even though some research shows that the stainless steel BPP on the cathode side might not require any coating without compromising the cell's performance, further studies are recommended on this topic [30].

2.2.2 Membrane Electrode Assembly (MEA)

The component between the half-cells of the PEM is the membrane electrode assembly (MEA), which is usually a thin (≈100 μm) Nafion solid membrane. This perfluorosulfonic acid (PFS) or polytetrafluoroethylene (PTFE) membrane is coated on both sides with electrode material [31], making it also known as a catalyst coated membrane (CCM).

The MEA's characteristics makes it a key-component on a PEM cell. Its chemical stability and high proton conductivity justify the high cost. Literature suggests that because the MEA's ohmic resistances can be reduced due to its low thickness, it can increase the efficiency of the system. Even so, the performance of the most known MEAs decreases at high pressure and temperatures. [22, 17] It is also the site for the chemical reaction and acts as an electrolyte, catalyst carrier and separator for the reaction gases. The electrode material consists mainly of catalyst and ionomer [17].

The placement of this component on the cell regards the anode and cathode side of the MEA, sites that match the coating of the corresponding catalysts: iridium on the anode, and platinum on the cathode side. Considering the materials that are normally used as a catalyst,

and since there is oxidation on the anode side at high voltage, the MEA must be resistant to high potentials (above 2V) [32].

In contrast, the MEA is often contaminated with metallic ions present in the BPP and PTL made of stainless steel, such as iron, chromium and nickel ions. Because of this, it is required to use deionized water (DI) as the environment for testing and run to improve the performance of the MEA, as well as an ion exchange resin that can capture any other ions from the process itself, making it impossible for those metallic ions to decrease the ionic conductivity [20]. In addition, Nafion changes its morphology due to destroyed sulfonic acid groups above 90°C [33].

2.2.3 Porous Transport Layer (PTL)

The gas diffusion layer (GDL), here porous transport layer (PTL), is the component of the PEM electrolyzer that is placed between the BPP and the MEA and must guarantee the homogenous current flow from the BPP towards the MEA. This characteristic is achieved by finding the best electric contact and removing the gases produced (mass transportation). Furthermore, the PTL should maximize water distribution over the active area of the anode side in case no flow-field structure is present in the BPP.

The following requirements need to be fulfilled by the PTLs:

1. Corrosion resistance at high overpotentials (> 2 V) in an acidic environment;
2. High electrical conductivity and no passivation during operation (low contact resistance with the BPP);
3. Good mechanical stability, mainly against hydrogen embrittlement on the cathode side;
4. Effective mass transport through optimal pore size distribution and porosity;
5. Low cost.

In addition, it must be considered that the structure of the PTL will highly affect the cell's performance, and so this component must endure at high current densities. Furthermore, the overpotentials and mass transport limitations (MTL) increase at higher current densities. In order of satisfying this problematic, the PTL is a high porosity structure having large pores capable of conducting electron transfer. The recommended porosities are 30 - 50 % with a pore size of 10 - 13 µm [33] so that the optimal lowest contact or ohmic resistance and best mass transport of the gases and water are reached.

2.3 PEM Electrolyzer's System Overview

The broad spectrum on PEM electrolyser systems counts on numerous stack and system designs, each one implemented to achieve the highest performance possible. Each design relies on flow diagram and feeds the PEM electrolyser. A simple example of this diagram is shown in Figure 2.3.

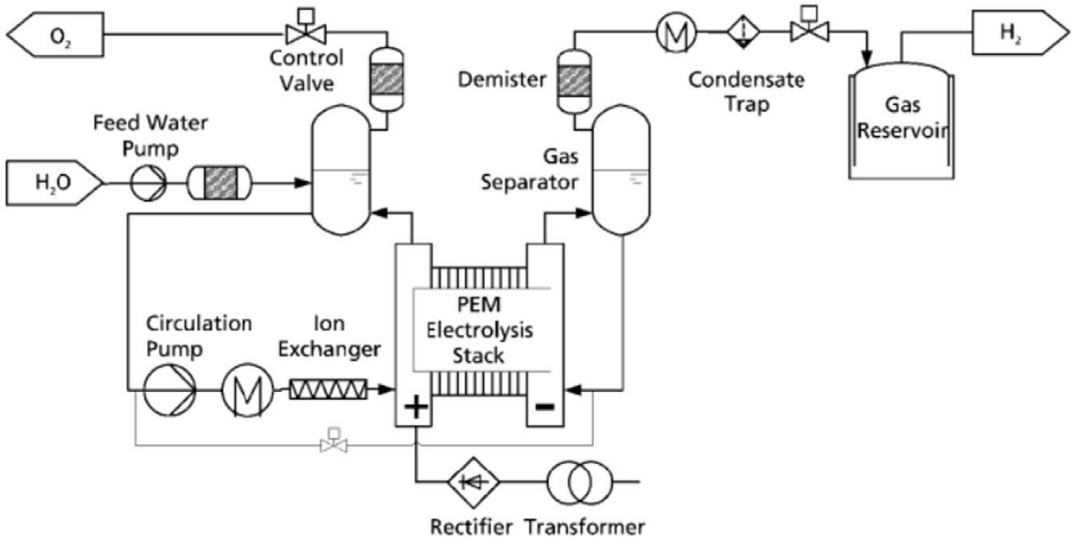

Figure 2.3 - Representation of a flow diagram of a PEM electrolyzer system [11].

Each system combines the power supply with the multiple feeding channels, a heat exchanger and the gas separator connected to the oxygen outlet that allows the water to be separated from oxygen. The circuit is lead at atmospheric pressure on the anode side, and the hydrogen leaves the electrolyzer through the cathode, where it is dried, compressed and then stored in a storage tank for further processing.

The commercial systems are generally operated between 40 – 80 °C and at 480 bar. Furthermore, most small plants are limited and have a maximum current density of 3 $A \cdot cm^{-2}$, resulting in a maximum efficiency of 75 % [11, 27]. Facing this range, the studies for materials and designs that can surpass these results are promising.

Focusing on cost reduction of PEM electrolyzers, research is based on component development in the materials of the MEA and PTL. In concern to the PTL, and recurring to recent studies, research on different types of materials indicate that those created by expanding the flat material and adding a metallic stack tissue show higher uniform electrical conduction on its structures [34]. These materials have different number of lines of tissue per area, wire diameters and pore sizes [35, 36].

Studies on stainless steel and titanium PTLs are carried out and come to conclude that titanium is a good option for this component, achieving better performances and lower corrosion [37].

In addition, it is possible to recur to precious metal coatings such as platinum to reduce contact resistance and thus increase cell performance [23, 34]. Since the surface of titanium PTLs are oxidized (passivation that increases the electric conductivity of the cell), it is necessary to study the interfacial contact resistance (ICR) created by the phenomenon. In fact, PTLs coated with precious metals have lower ohmic losses and electric contact as well as higher performance compared to other coating techniques [38]. The state-of-the-art coating of the cathode side is platinum-coated nanoparticles that are made of carbon from different companies such as ETEK /BASF, Tanaka and Johnson & Matthey. The catalyst loading of this material is 0.5 - 1 mg/cm^2. In the highly corrosive environment on the anode side, the choice is on iridium-based catalysts, even though ruthenium can also used due of its high activity [1].

Regardless, the choice for PEM electrolyzer stacks can often rely on which is the cheapest PTL on the market. With a choice of materials from meshes, felts, foams and sintered Ti structures, state of the art materials differ on mass transport limitations and corrosion.

Figure 2.4 demonstrates multiple materials and its SEM images to be used as PTLs.

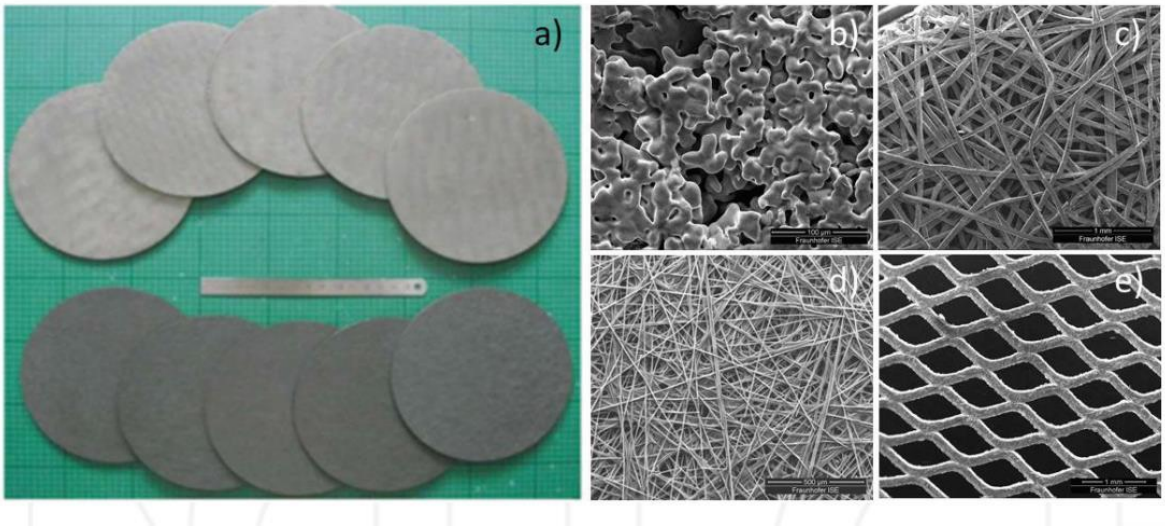

Figure 2.4 - Examples on materials for the anode PTL in a PEM electrolyzer: a) discs, b) sintered titanium, c) titanium felt, d) carbon, e) mesh (extracted from [29]).

While meshes are cheap, their mass transport limitations are significant. Sintered structures are optimised in its optimal contact area and highly effective, but very cost intensive. Nonwovens, foams and meshes have a higher contact resistance, but in contrast to sintered products, they can be varied in size and thickness. Another disadvantage of the nonwovens and foams is the reproducibility of the structures between the batches, which means that a constant pore size distribution and porosity cannot be guaranteed. The increased contact

resistance can be improved by means of a platinum coating, enhancing the need to further developments to reduce cost while keeping performance.

3 Materials and Methods

The focus on advanced electrochemical characterizations of PEM electrolyzer cells took different approaches along this research. After getting familiar with the electrochemical device, test benches, measurement equipment and the procedure of assembling an electrolyzer, there were detected a few technical difficulties that were quickly resolved by introducing new techniques or using other equipment or materials.

In an initial phase, electrochemical characterizations of the PEM electrolyzer cells were done for different compression pressure assemblies, using different torques in each assembly. The used compression pressures were as following: 0.2 N·m, 0.45 N·m, 1.0 N·m, 2.2 N·m and 3.0 N·m. It was necessary to confirm the calibration of each instrument, and it was possible to adjust to any difficulty and determine the optimal compression pressure.

In a parallel study, the electrochemical pre-characterization, polarization curves and EIS measurements were made for multiple PEM electrolyzer cells with different coated PTL meshes. Uncoated meshes were used as reference PTLs. After verifying and understanding the desired behaviour of each PTL assembly, it was necessary to adjust conditions and carry out at least three reproducible characterizations in order of generating error bars. Simulations using GeoDict were also conducted to link all results.

In a final phase, a service grid protocol was tested at operating conditions with the highest efficient PTL.

The work plan is presented in Figure 3.1.

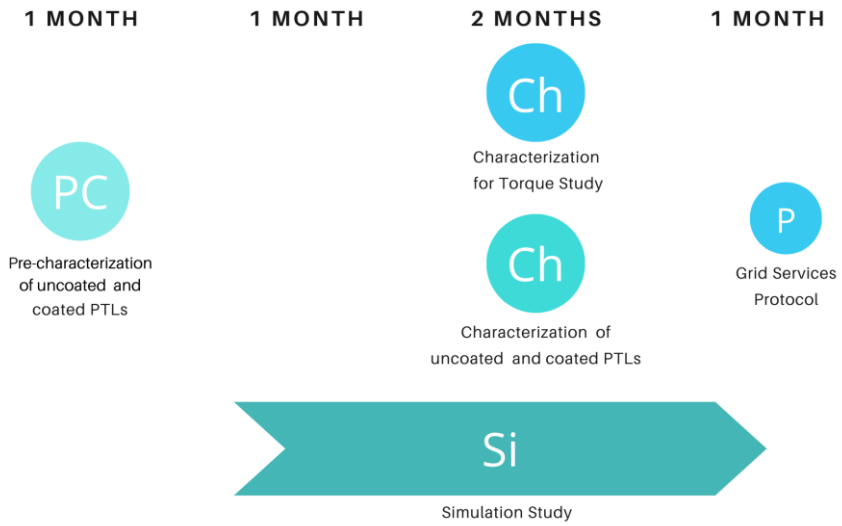

Figure 3.1 - Timeline and phases of the electrochemical characterization of the PTLs in the PEM electrolyzer cells.

3.1 Materials and Equipment

Each PEM electrolyser was prepared with the following materials: titanium and stainless-steel plates (BPPs), carbon paper TGP-H-90, Greenerity's commercial E400 CCM – MEA, used due to its stable with standard results, and the manufactured PTLs.

The BPPs were made without flow field and out of titanium on the anode side and either stainless steel or titanium for the cathode side. The carbon paper used for the assemblies was the TGP-H-090 from Toray with a porosity of 78 % and its cutting was done according to the necessary samples when needed, used to cloth the coated material and reduce the possibility of corrosion on the anode side [19].

The PTLs have a graded pore structure, with the fine-pored side being the contact area with the MEA. By combining the different pore sizes in a graded pore structure, the efficiency of the cell can be improved. Grigoriev et al. [33] showed that the cell voltage can increase up to 100 mV at 2.0 $A \cdot cm^{-2}$ due to insufficient pore structures, enhancing the need of an optimal pore structure for the efficient operation of a PEM electrolyser. The anode PTLs considered were as follows:

- Ti-GKN;
- Ti-Ti/Nb;
- Sintered Ti;
- Reference materials:
    - Ti-mesh;
    - Ti-GKN substrate.

The network structures of the PTLs examined consist of titanium with grade 3.7025. Ti-mesh reference sample was also used as support material for Ti-Ti/Nb and is commercially available-six-layer expanded metal from MeliCon GmbH. The arrangement of a stack also runs from coarse-mesh to fine-mesh to increase the removal of the gas bubbles by capillary forces. The second metal carrier is a single-layer titanium mesh with the same dimensions as that of the second layer from MeliCon GmbH. The coating on the Ti-Ti/Nb mesh was applied by VPS at DLR, previously cut and prepared. The layer consists of titanium with an additional niobium coating. Ti-GKN is a single-layer titanium mesh with a porous titanium, with a PM coating manufactured by DLR project partner GKN Sinter Metals and was provided for testing.

3.2 PTL Manufacturing (Coating Methods)

The coating of the titanium PTLs is produced by applying a MPL over a mesh. Its efficiency prevents the use of a sintered powder. There are different thermal processes designed for

this purpose, such as conventional flame spray, electric arc wire spray, plasma spray and high velocity oxy-fuel spray. They differ on the thermal and kinetic energy of the sprayed particles [39]. For example, the plasma spray is used for metal powders due to its higher melting points, as it is conducted at atmospheric conditions.

3.2.1 Vacuum Plasma Spraying (VPS)

Nevertheless, other coating methods can be used for different materials, such as Vacuum Plasma Spraying (VPS). The principle of this technique is based on a gas that flows between the anode and cathode side and gets ionized, and therefore forms a plasma torch, as illustrated on Figure 3.2 [39]. VPS is a thermal spraying process used for particles whose sizes are within the range from nanometres to hundreds of micrometres [40] and are propelled by a gas mixture of nitrogen, hydrogen, argon and helium and sprayed on a substrate. The temperature on this plume can reach 15 700 ºC [39] which makes the particles melt completely or partially, depending on the reached plasma enthalpy, and form a dense or porous coating, respectively.

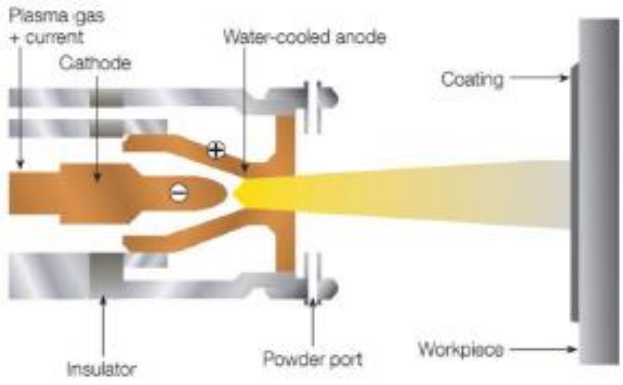

Figure 3.2 - Technique of VPS (extracted from [28]).

Using this vacuum process prevents the oxidation of titanium and corrosion of stainless steel substrates that are not desirable due their performances, and is used for coatings of solid oxide fuel cell and electrolyzers components, for electrodes for alkaline electrolysis, and coatings on BPPs and PTLs for PEM electrolyzers [40].

3.2.2 Powder Metallurgy (PM)

The powder metallurgy method (PM), also known as sintering, combines the production of metal powders and products from such powders using a process in a three process steps.

Firstly, a powder or powder mixture is submitted to a suitable pressing aid and then poured into a process tool. There, the mixture is pressurized at pressures on which the particles get

cold by welding. This creates a compacted structure that is submitted to a final step, on which the material is heated. The heating of this structure allows it to harden and strengthen to ensure further use since the individual powder particles combine with each other, ensuring that the component has enough strength.

Leading in thin components, the low-thickness powder layer can be fabricated by spraying a slip using a wet powder spraying process onto a substrate structure or by applying a powder slip using a doctor blade technique. Either way, the process must be finalized with a solidification step.

The greatest advantage of this method is its ability to use 95 % of the material submitted to the process, since the unmelted materials are recycled [41] and therefore resulting low material loss. Compared to this topic, the VPS coating method loses the material over the "over-spray" through the suction steps.

3.3 PEM Electrolyzer Assembly and Test Bench

The test bench was prepared to run testing on a single cell at the time, submerged in a DI water bath with > 0.1 $\mu S \cdot cm^{-1}$ of conductivity, at 90 ºC controlled by a heating plate and thermocouple within a hood to maintain the set conditions and also to ensure that produced gases are removed from laboratory in either case. The water source was always the same, so that the environment was never a field of study. The heating plate also allow an agitation stirrer of 300 rpm to be constant during testing.

Each PEM electrolyser was prepared taking account assemblies done previously with other studies run by DLR, and according to the scheme presented in Figure 3.3, where the components 1 to 3 belong to the anode side, as 4 to 6 belong to the cathode side.

The assembly of a PEM electrolyzer cell was done from the anode to the cathode side with an active area for the PTLs and the MEA of 4 cm^2. This area was guaranteed by aligning the materials and cutting the MEA slightly larger to prevent short circuit due to contact between the meshes. During the different phases of this research different assembly configurations were done, being those presented in Table 3.1.

Apart from the conditions of the bath, the assembly is also dependent on the condition of the materials. Cleaning the PTLs and the BPPs is an essential step to the best cell performance. The cleaning of the PTLs was assured by a primary cleaning step, in a 10 minutes ultrasonic bath in ultrapure water. The ultrasonic baths were done in a Bandelin Sonocool at 25 ºC. After a light polish, the PTL is put into a 10 minutes ultrasonic bath in isopropanol, followed

by a 5 minutes ultrasonic bath in ultrapure water that leads the meshes to the oven for drying. The set temperature of the oven was at each time 90 ºC.

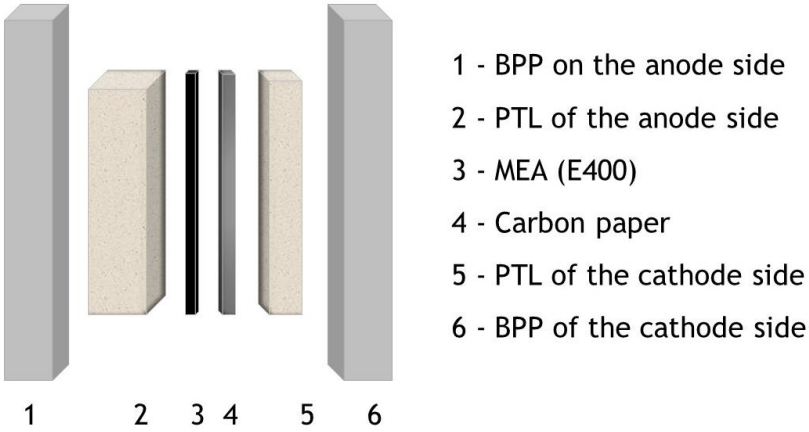

Figure 3.3 - Cell components and structure of a PEM assembly.

Table 3.1 - Cell configurations according to its corresponding work plan phase.

1	2	3	4	5	6
Pre-characterization					
Ti BPP	Ti/GKN	E400 CCM	TGP-H-090	Ti/GKN	Ti BPP
	Ti/GKN			SS-mesh	
	Ti mesh			SS-mesh	SS BPP
	Sint-Ti			SS-mesh	
Characterization					
Ti BPP	Ti substrate	E400 CCM	TGP-H-090	Ti substrate	Ti BPP
	Ti/GKN			Ti/GKN	
	Ti/ Ti mesh			Ti mesh	
	Ti/GKN	-		Ti/GKN	

In case of minimum mass transportation and no short circuit, only the primary cleaning was done between assemblies. The BPPs were cleaned by sanding the plates with 1200 sandpaper to remove the oxide layer formed on the coated titanium, followed by sanding with 4000 to 7000 SC to polish the mirror facing side of the plates, washing with isopropanol and water.

To close the cell, a torque key was used to cross tightening the screws and to guarantee more mechanical stability. Different tools were tested for calibration.

3.4 Scanning Electron Microscopy (SEM)

Figure 3.4 below shows the SEM images of the Ti uncoated and Ti-GKN PTLs of magnification of 100x for Ti mesh and 38x for Ti-GKN, made by Svenja Stiber at DLR. This imaging technique uses the emission and reflection of electrons that are detected and whose angle of inclination and intensity of the reflected secondary electron beam provide electrical signals are then displayed on the monitor as an image. The final image presents a black background that represents the epoxy resin used for the sample preparation. The elements with higher atomic mass are shown in lighter tones, taking the ones with low atomic mass to be represented in darker tones. In the samples in question this means that only the medium tone areas in sight and correspond to titanium.

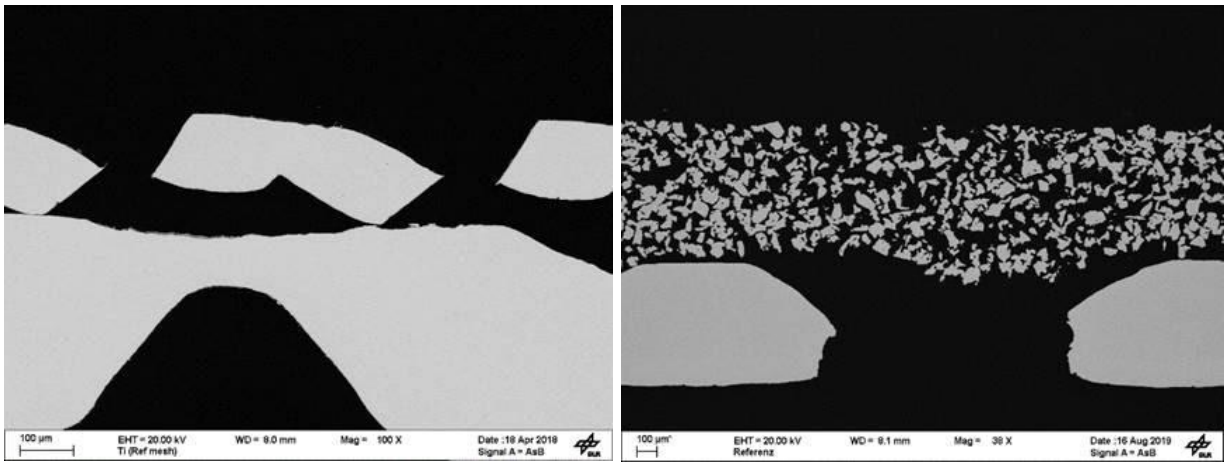

Figure 3.4 - SEM images of the Ti mesh (on the left) and Ti-GKN (on the right) PTLs.

Analysing both images makes it possible to admit that the Ti mesh PTL has a smooth and solid surface with a large-pore contact surface, since the PM coating can lead to a narrowing of the pores and a structured surface along the mesh, visible on the Ti-GKN PTL. In this material, the Ti-GKN layer follows through its entire surface and makes it more porous. Both samples show the titanium layer that is very dense and adheres very well to the titanium mesh.

The physical characterizations of these materials was previously studied by Aleyna Üstün at DLR, listing the porosity and the modal pore diameter of the Ti-GKN, Ti mesh and Ti-Ti/Nb PTLs. As confirmed, the VPS coating of the Ti mesh PTL reduces the modal pore diameter and the porosity of the samples. Even though this effect is not extremely visible considering these materials, this study becomes a relevant factor in the use of coated PTLs such as Ti-Ti/Nb, used in DLR studies. Furthermore, the high porosity visible in the SEM image is confirmed on Ti-GKN and Ti-Ti/Nb samples.

3.5 Physical Characterization

3.5.1 ICR Measurements

Improving the cell efficiency, as well as finding an optimal power supply, can also be approached by reducing the contact resistances of the PTLs. This parameter is studied by reproducing the interfacial contact resistance measurement (ICR), a physical characterization relevant in coated and uncoated PTLs.

This method relies on registering the cell voltage at a constant current density and multiple weights that then is used to calculate the resistance R, corrected.

The contact resistance measurement (physical characterization) was done by positioning the PTL sample with the carbon paper between two well-polished and gold-coated copper cylinders, connected to a potentiostat. Keeping the DC current constant at 1.25 $A \cdot cm^{-2}$ (5 A), the voltage was measured at different pressures. The experimental setup was placed between a hydraulic press, allowing the weight of the sample to vary from 20 kg to 200 kg in 20 kg increments. The voltage was translated into the resistance, being that the resistance associated with the PTL is the measured resistance with the correction of the gold-coated copper cylinder's resistance.

The ICR measurements were done for the following PTLs: titanium coated with GKN (Ti-GKN), stainless steel mesh (SS-mesh), titanium uncoated mesh (Ti-uncoated) and sintered titanium mesh. The samples were measured three times, each measurement with a new carbon paper.

3.6 Electrochemical Characterization

The electrochemical characterization of each configuration was done so that three assemblies whose polarization curves and EIS measurements presented the same behaviour would be considered.

3.6.1 Polarization Curve

One of the most used method for characterizing low-temperature electrolysis cells is the polarization curve or current-voltage characteristic curve. To enable harmonized component, cell and stack characterization, the Joint Research Center (JRC) published a protocol on recording polarization curves [42]. From this method it is possible to obtain a graphic representation of the response voltage over the specified current density from which it is studied information about loss mechanisms, such as mass transport limitations, reaction kinetics and ohmic resistances.

The interpretation of a polarization curve provides the understanding of the major contributions to the decrease of the real potential and any changes concerning the operating conditions since that decreases or increases on the cell potential can happen due to temperature, humidity, pressure and flow rates in the system. Figure 3.5 shows a typical course of a polarization curve, where all the losses explained in 2.1.2 are represented. Its interpretation focuses on multiple parameters: the slope of the polarization curve is given by the linear ohmic loss, while he activation processes mainly cause overpotentials at low current densities. Comparing these three areas of the graphic allows comparisons and conclusions to be made about kinetic losses of the PTLs, since the PTL structure governs over the mass transport capacity of the cell and therefore can cause an exponential rise in the curve at very high current densities [38].

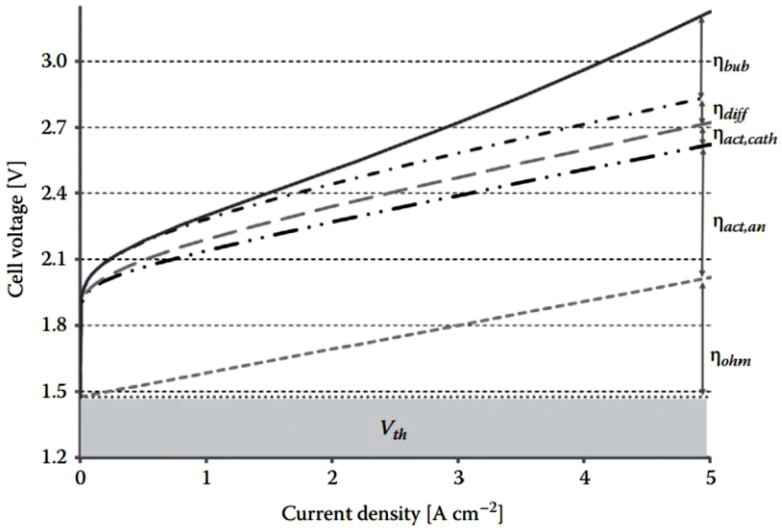

Figure 3.5 - Polarization curve (extracted from [26]).

The polarization curve is obtained under galvanostatic control, where is applied current (i /A) and the responding cell potential (V / V) is measured. The input current can be applied with a potentiostat or a power supply, where the potential is measured manually with a multimeter or with another relevant appliance. All measurements must be terminated when the cell potential reaches 2.4 V and a it should never surpass 3.0 V. Furthermore, it is necessary to stabilize the potential values by setting a time step in a manually mode or with a scanning rate with automatic mode, for correctly reading the potential values.

The desirable cell performance is achieved by the lowest cell potential possible [43].

For the electrochemical pre-characterization, each polarization curve was obtained by applying DC current with a TTi Power Supply from 0 to 2.0 A·cm^{-2}, according to the manual from Joint Research Centre and Fuel Cells and Hydrogen Joint Undertaking [42]. The polarization curves for the electrochemical characterization phase were obtained from 0 to 6.0 A·cm^{-2} or until the cell voltage was reaching 3.0 V as the limit.

3.6.2 EIS

Electrochemical impedance spectroscopy (EIS) is an electrochemical characterization method that evaluates the system response to a defined periodic sinusoidal excitation (AC) represented on a Bode or Nyquist plot.

Through this method, the inhibition processes (impedances, $Z\omega$) are illustrated through the system response, measuring the ability of a circuit to resist the flow of current and store electrical energy [44]. The impedance is a result of the ratio between the potential and current in a dynamic system for each frequency [24], as the equation 3.1 represents.

$$Z_{\mathrm{w}} = \frac{V_{\mathrm{w}}}{I_{\mathrm{w}}} \tag{3.1}$$

The results from these measurements result in a plot of impedances, with individual values for each frequency, which makes it possible to detect different processes that occur in each frequency range, from mechanisms, kinetics, structure and effects of degradation. For each measurement, the potentiostat connected to the cell sends out a sinusoidal alternating voltage (potentiostatic) or an alternating current (galvanostatic) to the system with a previously set amplitude and frequency range, parameters that also determine the duration of the measurement. To the chosen settings, the frequency is varied within its range and it is registered the resulting phase shift φ of the output signal which is translated into the impedance, Z, and represented in a Nyquist diagram, as shown in Figure 3.6, in a complex plane. The real part describes the active resistance, while the imaginary part defines the reactive resistance, responsible for storing energy.

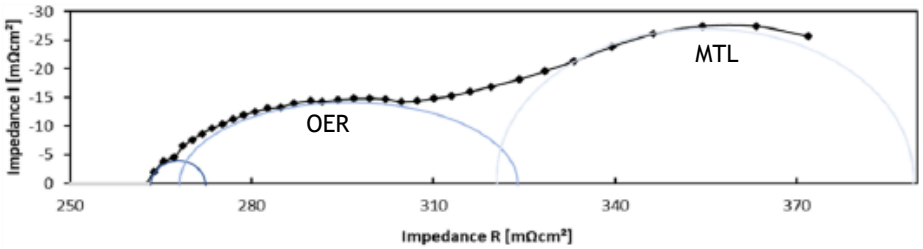

Figure 3.6 - EIS example measurement in a Nyquist diagram.

The impedance lines can be divided into the blue semi circles on Figure 3.7, so that each impedance can be determined and analysed. The equivalent electrical circuit diagrams of the system are simulated according to Figure 3.7, combining elements of resistances, capacitances and impedances, in series and in parallel.

The equivalent circuit consists of an inductive element L that is induced by the cable routing, and the series-connected ohmic resistor R. The two impedances lead to a shift of the zero point along the x-axis. Even though these elements are connected, there is a lack of research to support interpretations related to this matter, as it is possible to either connect the R /

CPE element as the first charge transfer of the two-stage oxygen evolution reaction (OER) [45], or put the responsibility on the hydrogen evolution reaction (HER) [19].

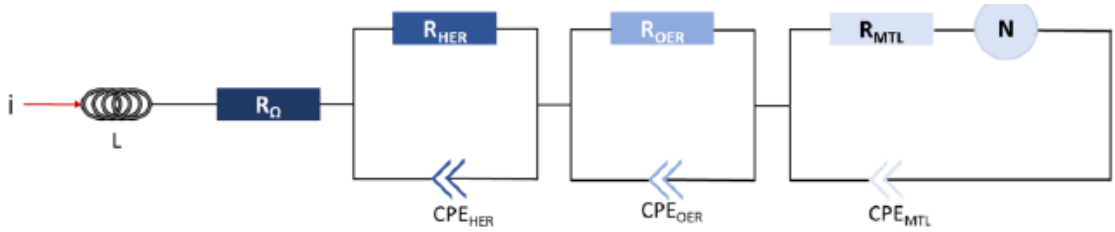

Figure 3.7 – Exemplary electrical equivalent circuit diagram of the system.

Nevertheless, each semicircle is dependent to a certain process. The first one is possibly dependent on HER, since it is not proportional to the second semicircle, responsible for the charge transfer resistances in HER [19]. The inexistence of relation between the semicircles breaks the possibility of the first one being dependent on OER. Even so, its connect to HER, charge transfer resistance, double layer effects in the electrode or the first charge transfer in OER [25]. The constant phase elements (CPE) is a measure of the non-ideal of a capacitance that is influenced by the surface roughness and the position of the components in relation to each other [46], making the assembly of the cell once again a key focus for its efficiency. The final R / CPE element is the Nernst element, connected to the losses of the MTL and any diffusion overpotentials [47]. It should be noticed that the ohmic resistance is regarded at high frequencies, in common with the activation losses, while the mass transport limitations are visible at lower frequency ranges.

Being a technique used in the study of catalytic reaction kinetics, diffusion of ions, corrosion, fuel cells, batteries and electrolyzers [48], EIS measurements enables an access to the cell's degradation and performance while the system is working, instead of analysing post-mortem data [44, 49].

The EIS was performed with an impedance module Zahner PP240 in galvanostatic mode with a frequency range from 100 mHz to 50 kHz of frequency and amplitudes between 50 mA and 500 mA. The input current was 1 A (0.25 $A \cdot cm^{-2}$), 4 A (1 $A \cdot cm^{-2}$) and 16 A (4 $A \cdot cm^{-2}$) for the pre-characterization measurements and 1 A, 4 A, 8 A (2 $A \cdot cm^{-2}$) and 16 A for the characterization measurements. The amplitude for each current density was kept similar in order of being able to compare the results from all trials.

After a polarization curve and EIS analysis is conducted, the results were analysed to check accordance between the same assembly configuration (trials) with the same parameters as mentioned before. After each set of measurements, the cell is reassembled, and a new configuration obtained after 3 successful trials.

3.7 GeoDict Simulation

In parallel to the characterization of PEM electrolysers, it was possible to use GeoDict as a simulation program. The access to this program was possible due to a partnership with the University of Esslinger, allowing the access to the computer with GeoDict's licence.

GeoDict is a simulation software developed by Math2Market for material property characterization, simulation-based material development, and optimization of processes through multi-scale 3D image processing, modelling and visualization of materials. Even though GeoDict can provide solutions within areas such as digital rock physics, electrochemistry and filtration, the simulations were run into the area of structural materials, exploring behaviours while considering properties such as thermal and electrical conductivity or thermal expansion. Therefore, the knowledge of these properties is a crucial part in both material and component development [50].

After conducting the necessary SEM images, it was possible to create three-dimensional geometric models, suited to perform simulations, characterization and modelling, through µCT images of the Ti-Ti and the Ti-Ti/Nb coated by VPS PTLs that allows a magnification of the images is 100x with a fine resolution. The µCT images for Ti-Ti/Nb and Ti-Ti were done with SkyScan2211 at Fraunhofer ISE in Freiburg, already in previous work, while the µCT images for Ti-GKN were developed with SkyScan1172 at the institute in Oldenburg. In a similar matter, this imaging technique uses the emission and reflection of electrons that are detected and whose angle of inclination and intensity of the reflected secondary electron beam provide electrical signals are then displayed on the monitor as an image. The final image presents a black background represents the epoxy resin that was used for the sample preparation and is assigned as a fluid in GeoDict. The elements with higher atomic mass are shown in lighter tones, taking the ones with low atomic mass to be represented in darker tones. This means that the brightest area corresponds to the Nb layer, since it is the heaviest metal in the samples, while the medium tone areas are stainless steel and titanium. The titanium mesh with Ti and Ti-Nb coating are presented in Figure 3.7 a) and b), respectively.

Even though both images presented some challenges due to its resolution, it was visible that the µCT images from the Ti-Ti PTL had some particles that didn't belong to the structure, making the simulation not reliable. To enhance the quality of these images and help GeoDict import the 3D structure, the pictures were edited by Tobias Morawietz.

Each importation had to consider the number of pictures enrolled in the importation folder, as well as image pixel size and exposure. Furthermore, it was necessary to increase image quality through implementing the following filters, applied in image processing: sharpen filter, with a strength of 35 % within the first threshold, twice taken into the image and

responsible to add contrast to the image, as well as soften lost particles non related to the structure; non-local means filter, with a strength of 100 and within the patch radius of 1 voxel (automatic argument designed by GeoDict) for noise reduction [51]; and the thresholding outline segmentation visible. This allowed each threshold limits, that is, each material component to be delineated. An example of the resulting import can be found in Figure 3.9.

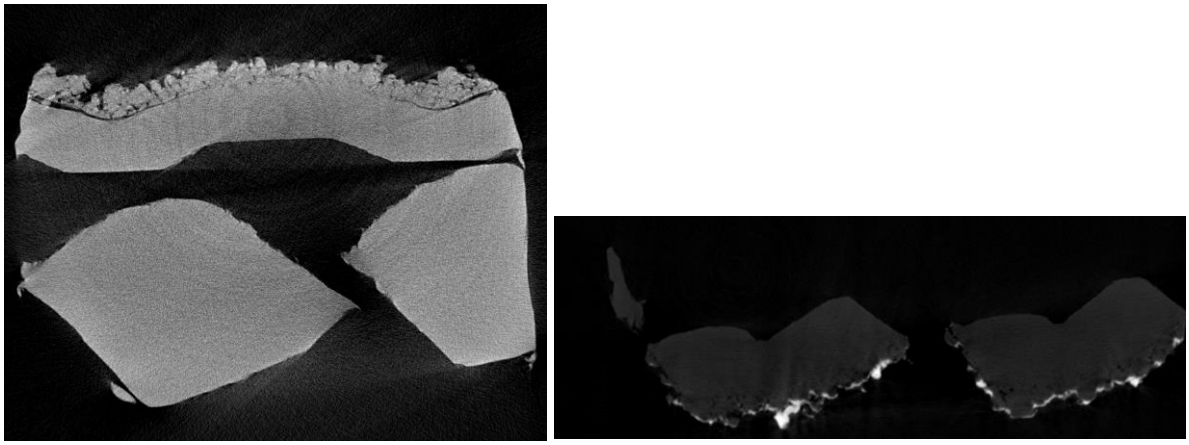

Figure 3.8 - µCT images of samples from: a) Ti-Ti; b) the Ti-Ti/Nb coated PTLs.

Taken each PTL sample, GeoDict allowed to run a simulation considering different modules: PoroDict, where it is possible to analysis of the pore space taking into account geometric pore size distribution, pore size distribution by porosimetry and percolation path; DiffuDict, where the tortuosity factor and the effective diffusivity of porous media are computed; and StatuDict, where it was analysed the capillary pressure curve [52].

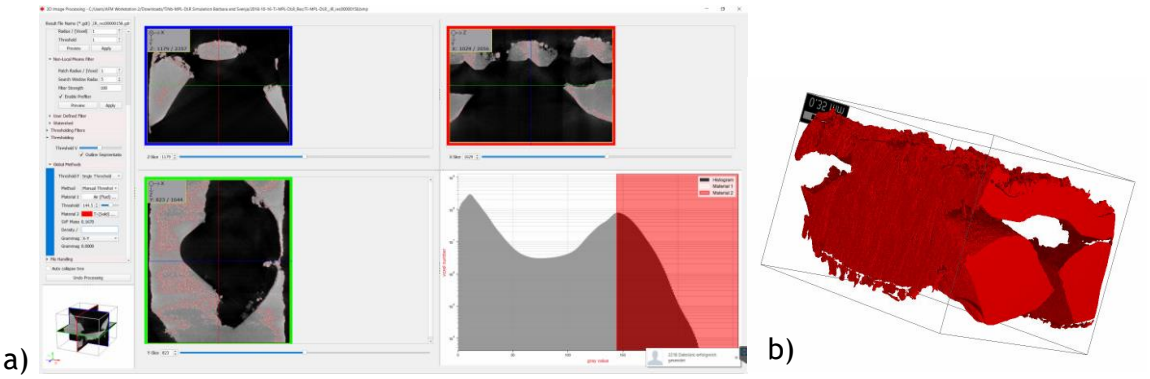

a) b)

Figure 3.9 – a) Import screenshot of GeoDict structure; b) 3D representation of the import.

Within PoroDict it was analysed the bubble point which is calculated on basis of the largest through pore and the Young-Laplace-equation and the number and volume of open and closed

pores, while StatuDict predicted the capillary pressure curves and DiffuDict analysed the tortuosity factor. These properties are possible to predict with a considerable quality due to the coating being done by VPS (Ti-Ti/Nb) and PM (Ti-GKN), which allows them to be controlled in the process [28].

The bubble point is the necessary pressure for the water reaches the largest pore along a certain direction, going through the structure and available pathway [19] and is calculated on basis of the largest through pore and the Young-Laplace-equation [52]. The tortuosity factor is a diffusion and flow characteristic that evaluates the convoluted pathways of the structure, as a measure of complexity of the pore space. Finally, the capillary pressure curve registers the capillary pressure over pore saturation, whose analysis, in addition to the bubble point, can help evaluate overvoltages [19].

4 Results and Discussion

In this chapter, all results from the characterizations are presented, analysed and discussed. So that all data could be compared, the third trial of each measurement was the one considered throughout this chapter. The data from the first trials was considered in the error bars present in the plots. The lines in the plots were added for better visualization of the results.

4.1 Evaluation of the Characterization with Different Compression Pressures

The characterization of cells at different compression pressures was done in similar conditions to those desired for the characterization of the following PTLs: Ti mesh, Ti-GKN and Ti-GKN substrate, a material created by removing the coating of Ti-GKN and sanding its surface. Each measurement followed by applying a higher pressure to the assembly and submitting the same configuration to another set of tests, safeguarding the absence of short circuits.

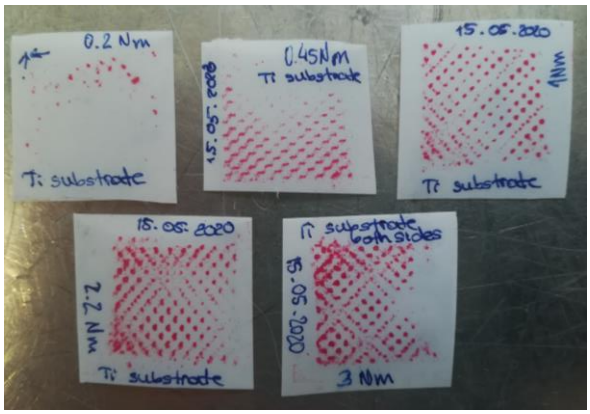

Figure 4.1 - Pressure foil images at the different compression pressures with cell assemblies using Ti substrate as the PTL.

In addition to the torques calibration, pressure foil testing was also performed. The images produced by compressing pressure foil between the PTLs is shown in Figure 4.1 and illustrate how the different torques behaved. The necessary adjustments at the compression of the cells were done so that this pressure applied would be homogeneous.

The polarization curves up to 4.0 $A \cdot cm^{-2}$ resulting of this study are shown in Figure 4.2, below.

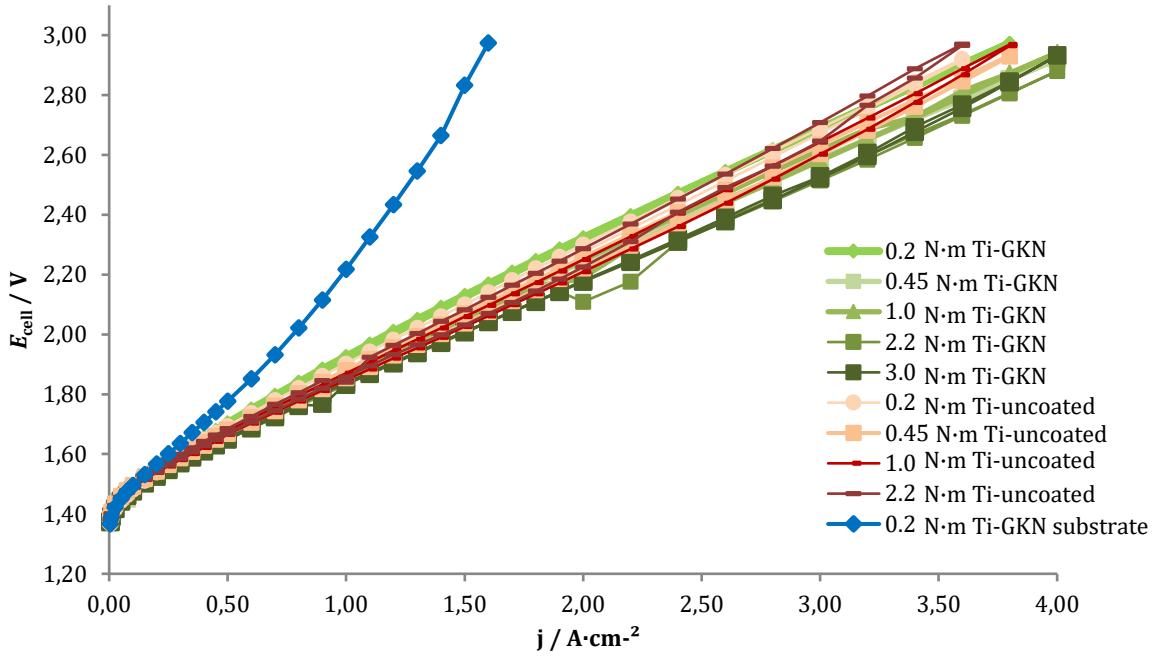

Figure 4.2 - Polarization curves of the different cell assemblies for multiple compression pressures up to 4.0 A·cm^{-2} at 90 ºC.

A more detailed illustration of the polarization curves represented in Figure 4.2 can be found in Appendice A.

The samples of the Ti-GKN substrate evidence a very unstable assembly, with short circuits occurring frequently. Its poor performance is not surprising since these samples are not designed as a material for PTL itself, but as a coating material. The analysis of the polarization curves over their linear courses allows conclusions about the overpotentials of each PTL, in further detail in 4.2. The best performance was achieved by using Ti-GKN, being also the only material on which it was possible to operate with a 3.0 N·m compression pressure. In a comparative layout, the cell performance values of each PTL at 2.0 A·cm^{-2} for the various compression pressures are presented on Figure 4.3.

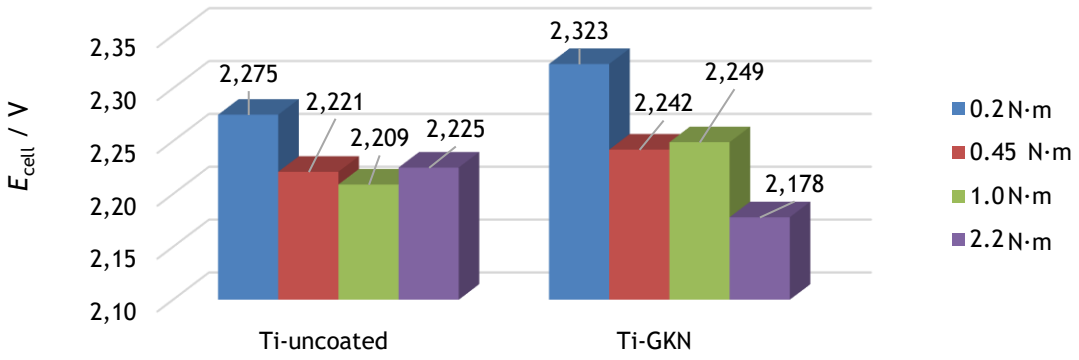

Figure 4.3 - Cell performances at different compression pressures and a current density of 2.0 A·cm^{-2}.

A higher cell performance is reached by increasing the compression pressure, consequently increasing the contact area. This course is limited, however, since that with pressures higher than 2.2 N·m the cell performance can be unstable at higher current densities and portrait higher losses and short circuits due to mechanical stress [53].

The EIS measurements are shown in Figure 4.4 as a Nyquist plot at 0.25 A·cm^{-2} of the samples.

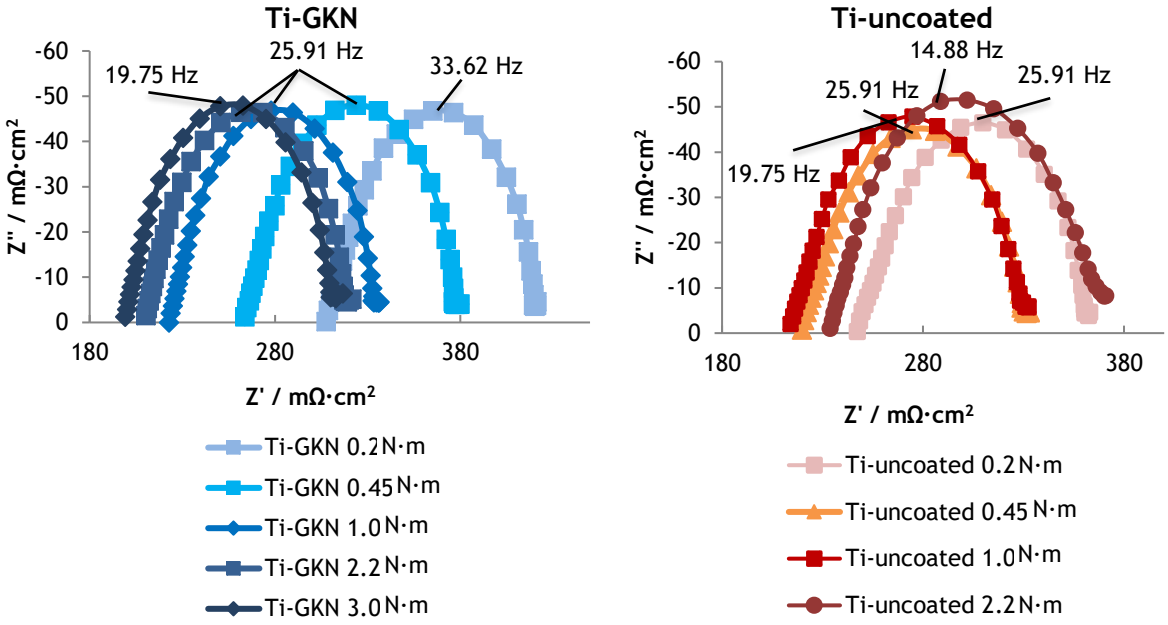

Figure 4.4 - Nyquist plots from the EIS measurements at 0.25 A·cm^{-2} with an amplitude of 100 mA and a frequency range from 100 kHz to 50 mHz.

As shown through the polarization curves, the Ti-GKN has a wider gap between the different cell performances at each current density, resulting in different resistances as a function of the compression. The ohmic resistances of the Ti-GKN are 308 mΩ·cm², 264 mΩ·cm², 223 mΩ·cm², 210 mΩ·cm² and 199 mΩ·cm² for the pressures of 0.2 N·m, 0.45 N·m, 1.0 N·m, 2.2 N·m and 3.0 N·m, respectively. The ohmic resistances of the Ti mesh PTL take values of approximately 247 mΩ·cm², 220 mΩ·cm², 214 mΩ·cm² and 234 mΩ·cm² for the pressures of 0.2 N·m, 0.45 N·m, 1.0 N·m and 2.2 N·m, respectively. At higher compression forces, the ohmic resistances decrease, consequently increasing the cell performance. The odd value of 234 mΩ·cm² as Ti mesh's ohmic resistance can be explained by improved electric connectivity, resulting in values close to the ones with 1.0 N·m as compression pressure.

At the current density of 4.0 A·cm^{-2} the MTL is the determining factor, and mostly visible on the Ti mesh PTL. It was not possible to reach values up to 4.0 A·cm^{-2} for the Ti mesh other than 1.0 N·m. For this reason, Figure 4.5 shares the EIS measurements at 2.0 A·cm^{-2}.

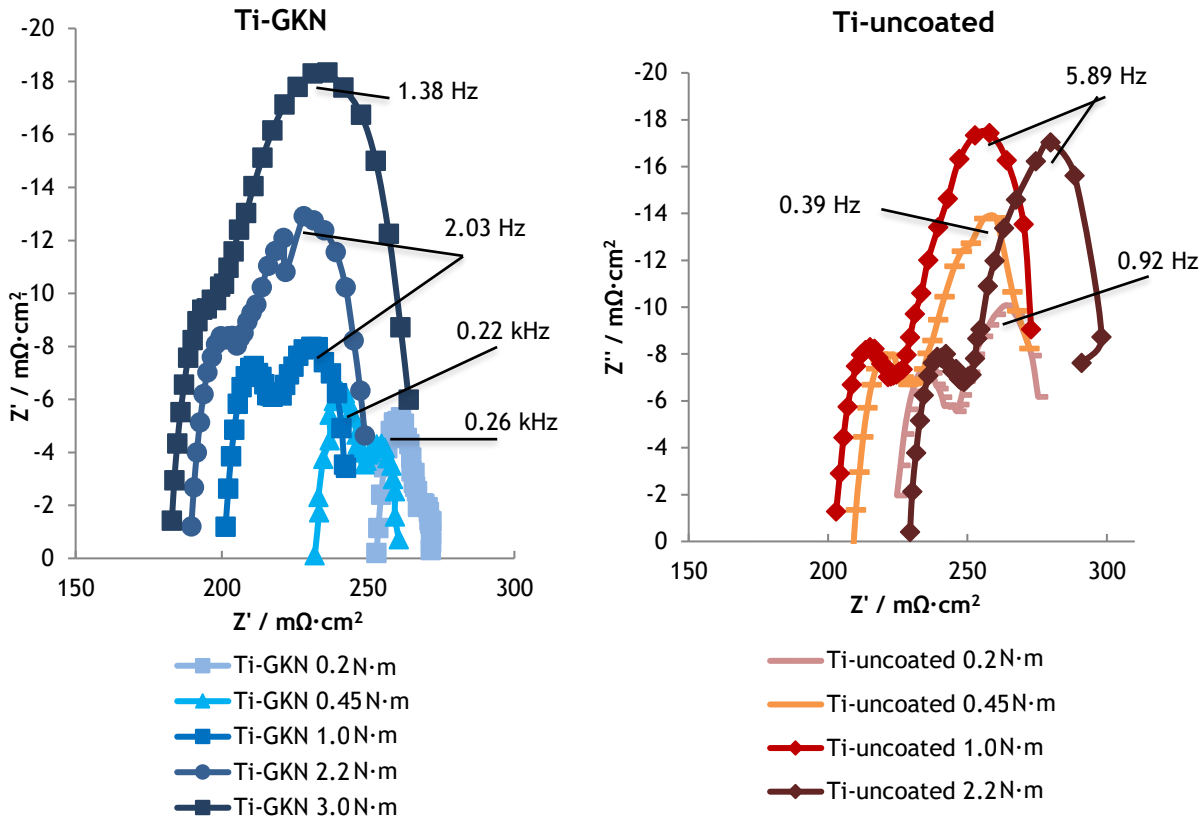

Figure 4.5 - Nyquist plots from the EIS measurements at 2.0 A·cm^{-2} with an amplitude of 200 mA and a frequency range from 100 kHz to 50 mHz.

In the Ti mesh PTL, the limitations dominated by the slow rate of activation of the OER decrease up to 1.0 N·m but tend to return at higher compression pressures. Likewise, it is only possible to stabilise the cell performance at high current densities with compression pressures up to 1.0 N·m. This can be explained by the pore contact area, being that increasing compression consequently increases the area available to lodge the gas bubbles created by the reaction. Despite this, at a certain pressure the MTL become higher than the porosity benefits.

In conclusion, 1.0 N·m should be the compression pressure used for cell assemblies, since higher values stress the cell mechanically too much and with lower values the performance is not desirable.

4.2 Evaluation of the Physical Characterization (ICR Measurements)

ICR measurements were performed to investigate the interfacial contact resistance of the component within a cell. As explained in the previous chapter, this phenomenon plays to the semiconducting property of oxide layers on the titanium [44] and explains why the Ti-GKN curve runs below the other PTLs. Nevertheless, in the absence of measurements done before

and after the materials are used for testing, the effect over the oxide layers cannot be observed [28].

Instead, the contact resistances (ICR) of the PTLs were measured and plotted against the clamping force (contact pressure), being that the high ICR value with low clamping force is gradually decreasing with increasing force. The results are shown in Figure 4.6.

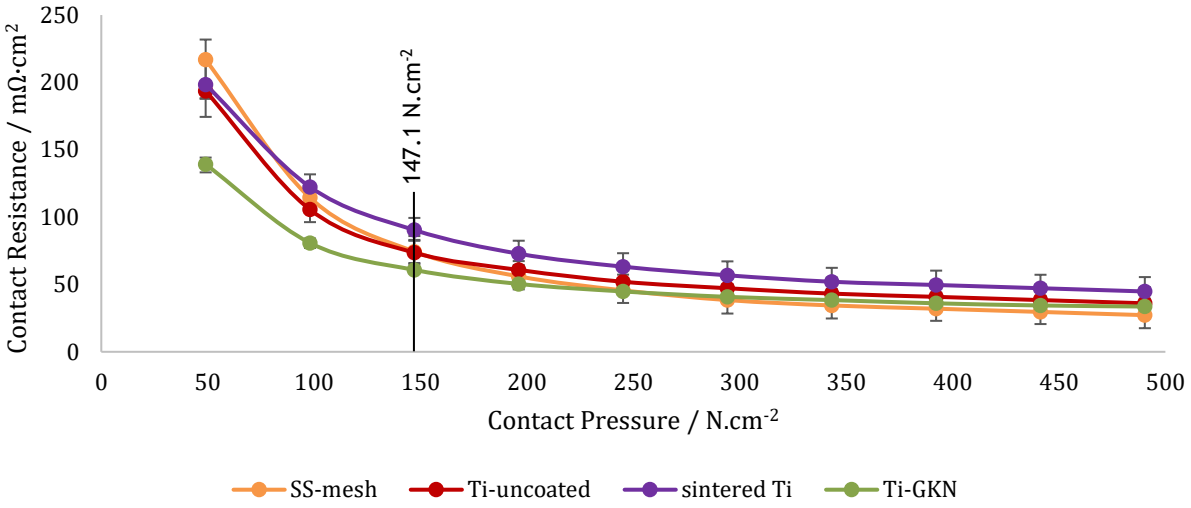

Figure 4.6 - ICR measurements for the SS-mesh, Ti mesh, sintered Ti and Ti-GKN PTLs.

The Ti-GKN has proven to demonstrate the lowest ICR at 147.1 N.cm^{-2}. Being the closest value to the compression pressure in the cell assemblies (100 N.cm^{-2}), it's worth a closer comparison at this contact pressure. On one hand, as explicit in Figure 4.7, the ICR takes the value of 60.8 mΩ·cm² for Ti-GKN, being the lowest value of all measurements. This low value confirms the conductivity of the material, despite of its high porosity. On the other hand, the sintered titanium PTL has the highest ICR of 90.4 mΩ·cm². This discrepancy can be explained by the reduced pore diameter as a result of the PM coating, as well as by the enhanced electron transportation in Ti-GKN due to the increased contact area.

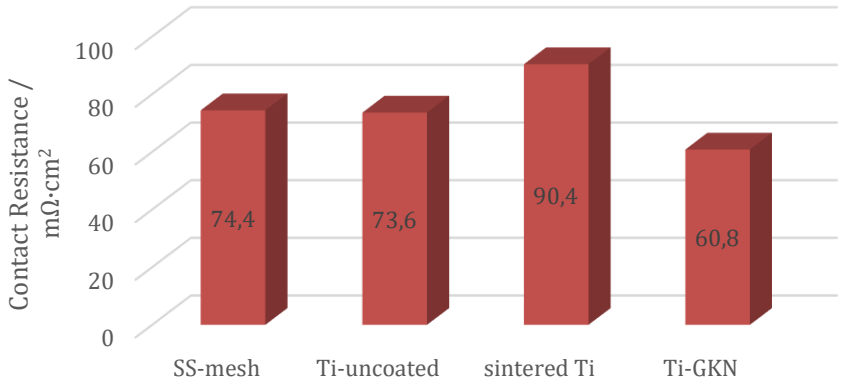

Figure 4.7 - ICR measurements for the SS-mesh, Ti mesh, sintered Ti and Ti-GKN PTLs for 147.1 N.cm^{-2}.

4.3 Evaluation of the Electrochemical Characterization

In a pre-characterization phase, the polarization curves of the multiple PTLs were measured up to 2 A·cm^{-2}, taking into consideration the configurations presented in Table 3.1, and where the efficiency of a PEM electrolyzer is related to the cell potential as the lowest potential values are translated into higher efficiencies. Figure 4.8 presents these characterizations.

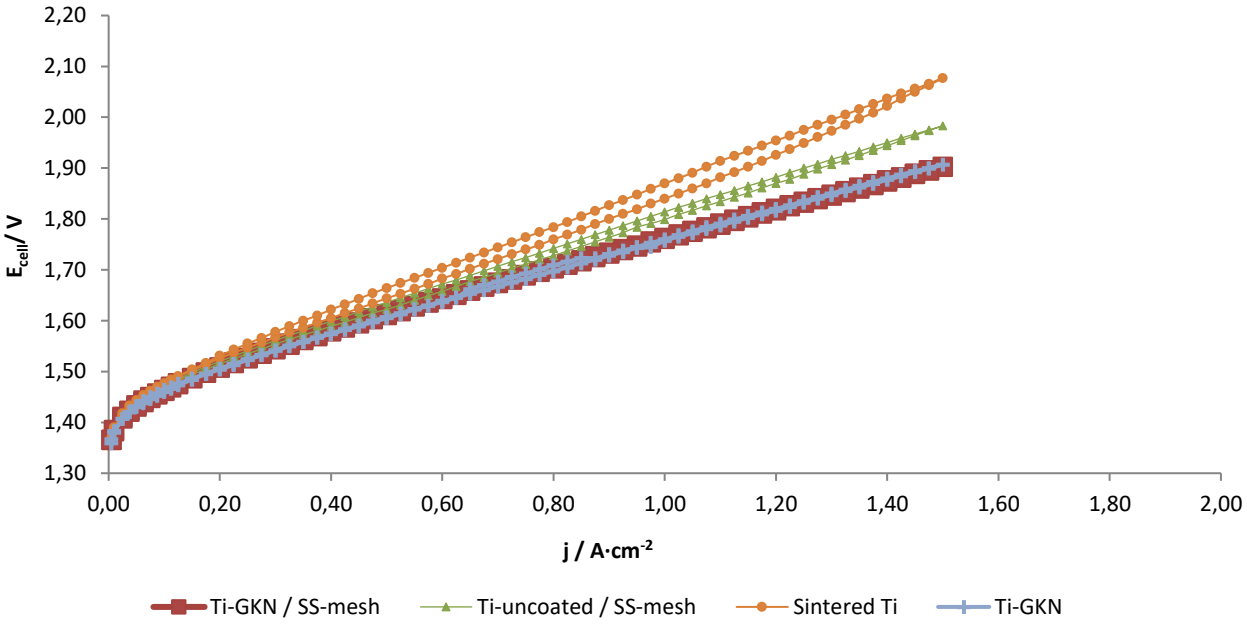

Figure 4.8 - Polarization curves of the different cell assemblies up to 2.0 A·cm^{-2} at 90 ºC.

Even though that at low current densities (up to 0.3 A·cm^{-2}) the polarization curves barely show any differences, at medium current densities, j, there are higher discrepancies and the differences imposed by electric control over the PTLs limitations are visible.

The polarization curves demonstrate the behaviour and slope for each PTL. The best performance was achieved by using Ti-GKN while the sintered Ti sample shows higher MTL identified by the hysteresis curve as well as slight exponential trend, since this deviation is connected to non-steady state conditions and MTL [19].

2.01 V was reached by the sintered Ti and 1.98 V by the Ti mesh at 2.0 A·cm^{-2}, while the Ti-GKN curves reached 1.90 V at the same current density.

Given the results achieved in this phase, further characterization of Ti mesh and Ti-GKN PTLs was designed. For comparison between coated PTLs, it was included a titanium PTL coated by VPS with a mixture of titanium and niobium (Ti-Ti/Nb). The polarization curves of these PTLs were measured up to 4 A·cm^{-2}, taking into account that the cell voltage must never surpass 3.0 V. Figure 4.9 presents the final characterizations.

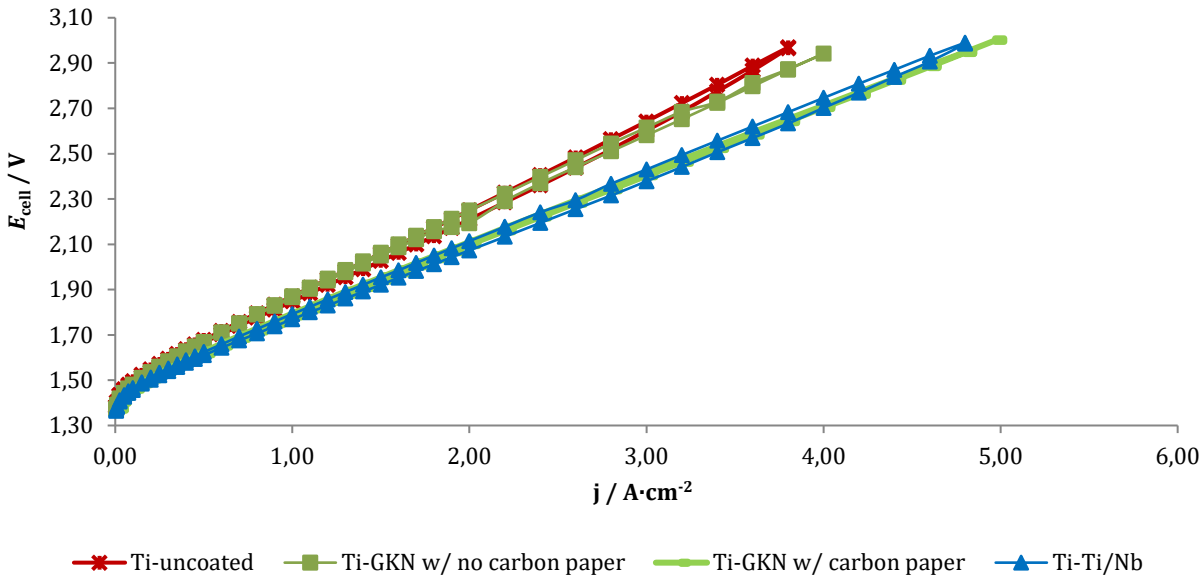

Figure 4.9 - Polarization curves of the different cell assemblies up to 6.0 A·cm^{-2} at 90 ºC.

At 4.0 A·cm^{-2}, the samples achieved approximately 2.70 V for Ti-GKN and Ti-Ti/Nb, while Ti mesh couldn't reach such current density, achieving a maximum of 2.97 V at 3.8 A·cm^{-2}. Furthermore, the linear course of Ti-GKN at higher current densities, as well as hysteresis on the Ti-Ti/Nb curve, suggest low mass transport limitations, state on which the overvoltages are studied with the help of EIS. The structure and porosity of the Ti-GKN PTL offers a better performance through an efficient mass distribution. The gap between the two-way curve of the Ti mesh PTL implies MTL on its surface. The best performance was achieved by using Ti-GKN as the PTL and carbon paper on the cathode side, with 2.70 V at 4.0 A·cm^{-2}.

It was possible to obtain more information about the ohmic and mass transport resistances by the EIS images, confirming the course of the polarization curves. Figure 4.10 shows the EIS recordings as a Nyquist plot with the equivalent circuit diagram in Figure 3.3 at 0.25 A·cm^{-2}.

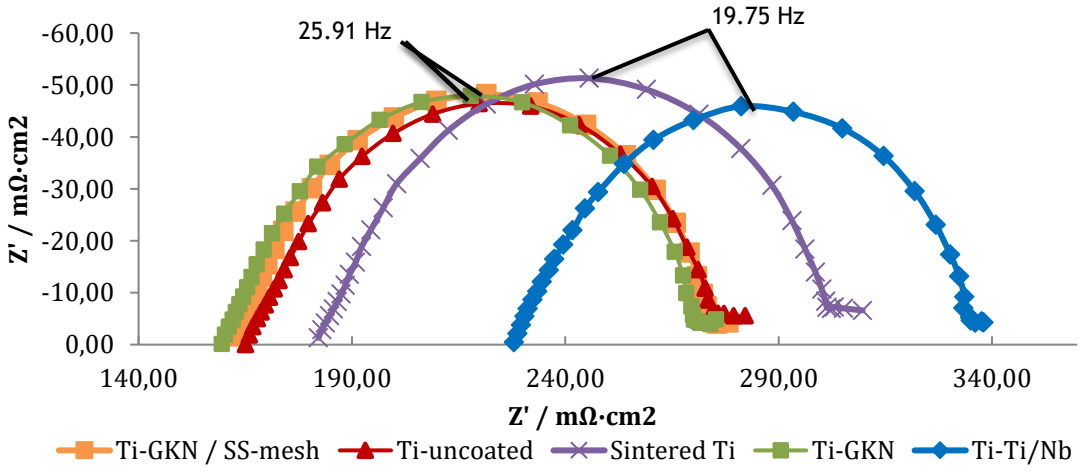

Figure 4.10 - Nyquist plots from the EIS measurements at 0.25 A·cm^{-2} with an amplitude of 100 mA and frequencies from 100 kHz to 100 mHz.

Each curve is represented as a semicircle whose peak occurs at a frequency on which the charge transfer resistance due to OER is most significant and their intersections on the real part axis differ due to their different resistances. Ti-GKN has an ohmic resistance of 159 mΩ·cm², comparable with Ti mesh, while the ohmic resistances for sintered Ti and Ti-Ti/Nb take values of approximately 182 mΩ·cm² and 228 mΩ·cm², respectively. In fact, these results confirm the mass transportation limitations suspected by analysing the polarization curves, showing ohmic resistances at low current densities, since in packed structures such as sintered Ti the water is not able to reach the active centers at the necessary rate [19]. This deduction also validates the results the ICR measurements.

If on one hand, at a current density of 0.25 A·cm^{-2} the limitations are dominated by the slow rate of activation of the OER; on the other hand, at the current density of 4.0 A·cm^{-2} the MTL is the determining factor. Thus, EIS measurements at high current density were performed to see the impact of mass transport limitation for the different PTLs which are shown in Figure 4.11 for samples that achieved the highest current density.

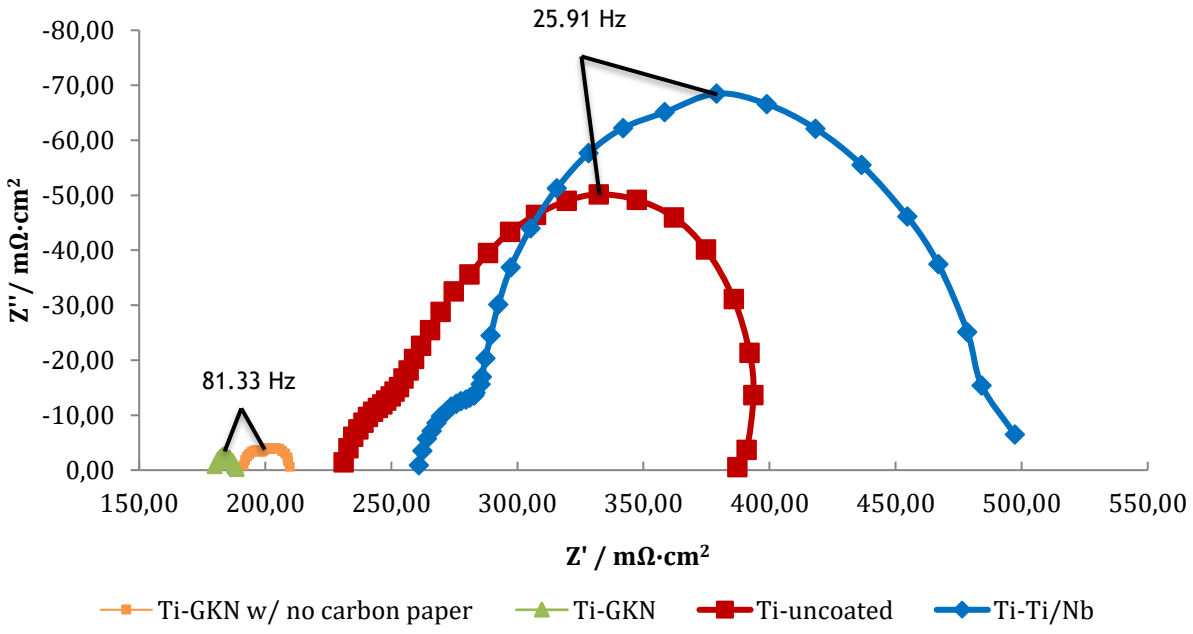

Figure 4.11 - Nyquist plots from the EIS measurements at 4.0 A·cm^{-2} with an amplitude of 500 mA and from frequencies 100 kHz to 50 mHz.

This major difference in the MTL resistances is the result of the larger pore contact structure of the uncoated PTL. In this structure the capillary forces are driven by a weak pore gradient because the gas bubbles are discharged at a limited extent. In the case of T-Ti/Nb, the mass transport is carried differently, where at elevated current densities the mass transport is not reached at an efficient rate. On the other hand, the porous layer of the Ti-GKN assures a more efficient gas removal, and therefore justifying its low resistance of 188 mΩ·cm².

It is also visible that the intersection with the axis of the Ti mesh sample shifts to the right by increasing the current density, instance the increasing ohmic resistance. In addition, the two semicircles visible in Ti-Ti/Nb and Ti mesh suggest limitations due to blocked active sites [19].

By comparing the characterization results the Ti-GKN is the PTL with the best performance, taking its place as a powerful PTL in the market. Its cell performance can be explained by the superior electron and mass transportation, as well as the minimized loss processes at current densities higher than 0.3 $A \cdot cm^{-2}$ when compared to other PTLs. This becomes the material of choice for further studies with current densities higher than 2.0 $A \cdot cm^{-2}$.

4.4 GeoDict Simulation Results

In response to the solver programmes described in Chapter 3, it was analysed the bubble point and the tortuosity factor, as well as predicted the capillary pressure curves of each coated PTL. Since the characterization for Ti-Ti was not done, the full results are showed in Appendix B. The values of the bubble point and tortuosity factor for Ti-Ti/Nb and Ti-GKN are shown in Table 4.1, while Figure 4.12 presents the capillary pressure curves.

Table 4.1 - Bubble point and tortuosity factor of the Ti-Ti/Nb and Ti-GKN PTLs.

	Ti-Ti/Nb	Ti-GKN
Bubble Point (Pa)	810.91	854.42
Tortuosity Factor	2.24	2.17

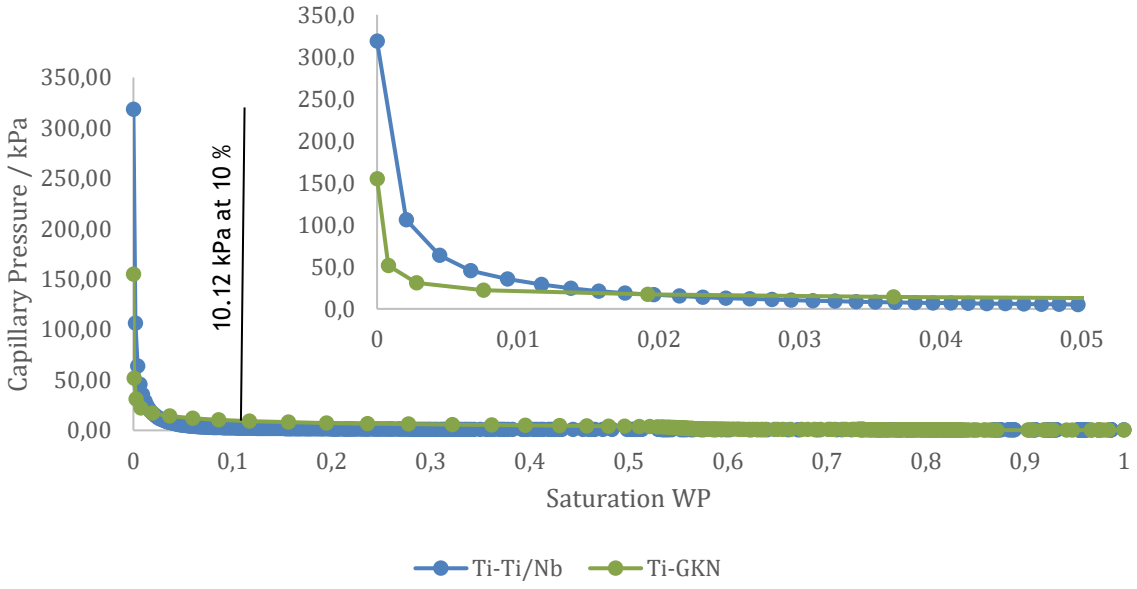

Figure 4.12 - Capillary pressure curve of the Ti-Ti/Nb and Ti-GKN PTLs.

The results are within the expected range according to other on-going studies and publications, as well as the characterization values. Ti-GKN has the lowest capillary pressure and tortuosity factor, as the ohmic resistances and MTL are not significant in relation to a soft slope in its polarization curve. The determined capillary pressure for Ti-GKN at a 10 % saturation is 10.12 kPa, while the capillary pressure for Ti-Ti/Nb is 2.37 kPa at the same saturation. The morphology of Ti-GKN provides higher values for capillary pressures with increasing saturation, which means that this material needs higher pressures to achieve a saturation state than Ti-Ti/Nb. Nevertheless, the saturation process starts at lower pressures, demonstrating the availability of the pores. These results are consistent to the performed characterizations, since they conclude that the gas bubbles are discharged at a limited rate.

Meanwhile, the Ti-Ti PTL shows elevated capillary pressures which can relate to high MTL [19]. With bubble point and tortuosity factor close to Ti-GKN, assumptions about overvoltages cannot be done about Ti-Ti/Nb, as these values are not higher due to the thickness and porosity of the sample and structure imported. Proved by physical characterization, this material has larger pores than Ti-Ti/Nb, which allow the particles to go through a path more easily, consequently leading to lower tortuosity.

Despite of the favourble results, this simulation study lacks other perspectives. Since GeoDict multiplies the imported structures to create a greater volume, an interesting work can be by cropping the 3D structures to optimize the pore radius resulting from the simulations to value similar to the one indicated by the porosity study mentioned at the beginning of this chapter.

4.5 Availability for Grid Services

A dynamic operation studies performance evaluates the response time under operating conditions. The chosen testing protocol is an evaluation of the electrolyzer performance to frequency control reverse (FCR) service grids and its phases are illustrated on Figure 4.13.

The protocol was carried out by recording data every 15 seconds, and considering the power reached by Ti-GKN on the characterization phase of this study. So, the upper power level, P_{up}, is set with a current density of 4.0 $A \cdot cm^{-2}$; the lower power level, P_{low}, is the set by the minimum current density possible, approximately 0.0 $A \cdot cm^{-2}$, and the medium power level, P_{med}, is set with a current density of 2.0 $A \cdot cm^{-2}$. A closer look at the response for the steps at 4.0 $A \cdot cm^{-2}$ can be seen on Figure 4.14, where it is visible that the potential increases with time. Due to changes such as response of the catalyst material and oxidations, the voltage increases, until stabilizing after an expected 200 hours on which is system is conditioned. In addition, the constant switches of current densities in short period of times prevent high degradation rates, balancing moments of improvement and degradation.

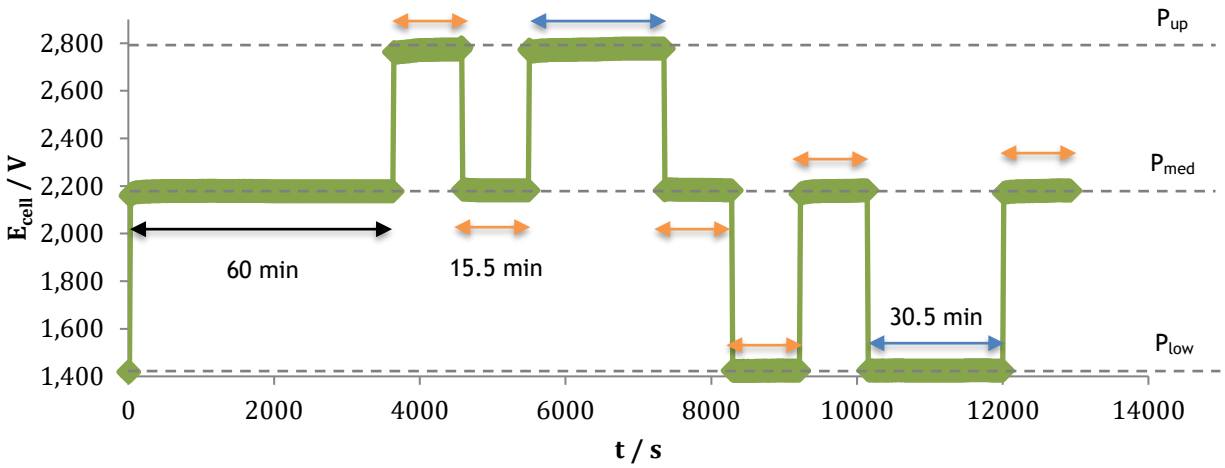

Figure 4.13 - Grid services protocol (response, phases and parameters).

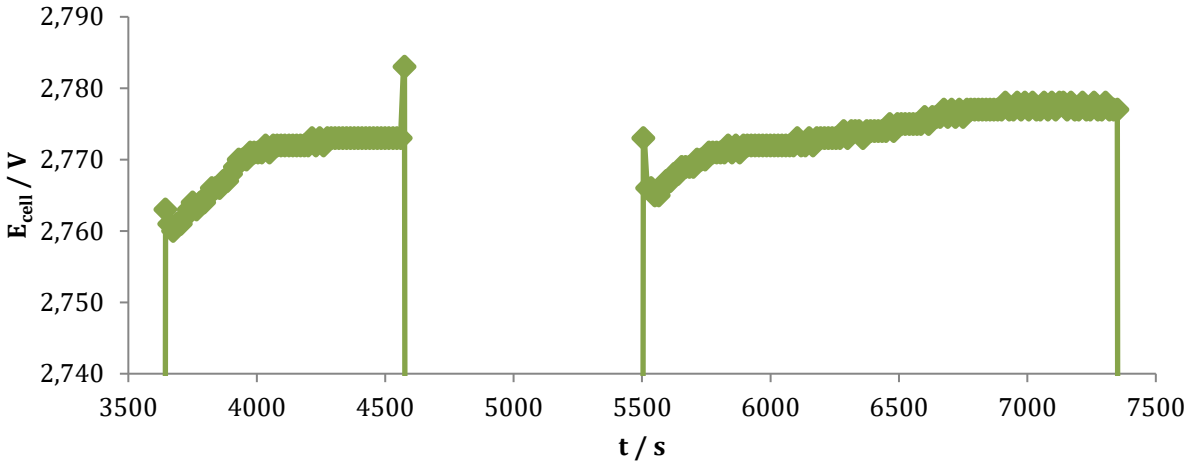

Figure 4.14 - Grid services protocol response at 4.0 A·cm^{-2}.

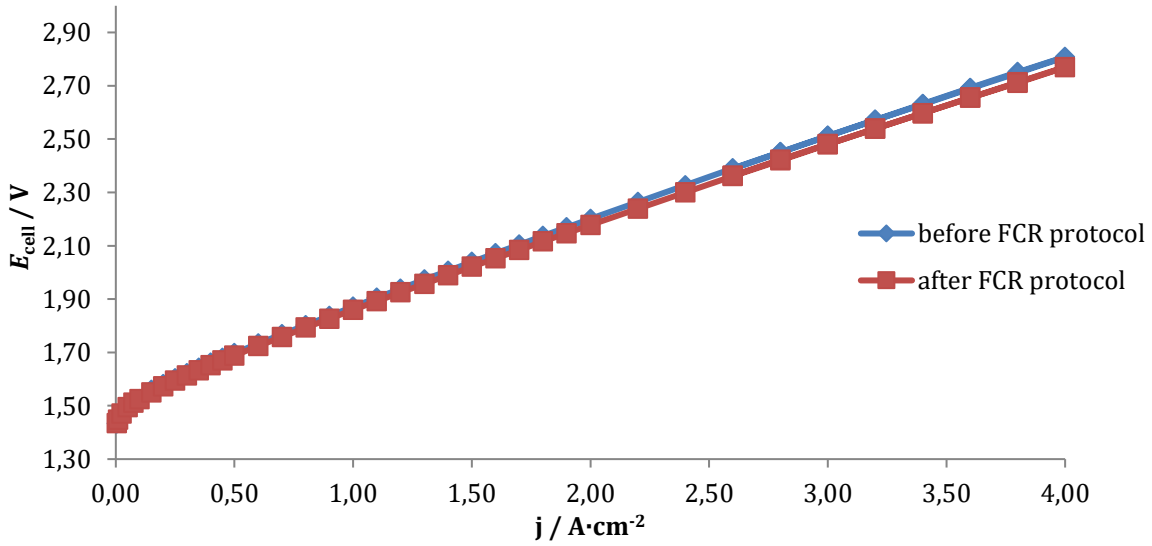

Figure 4.15 - Polarization curves of Ti-GKN up to 4.0 A·cm^{-2} at 65 ºC before and after the protocol.

The polarization curve and EIS measurements performed before and after the FCR protocol are shown in Figures 4.15 and 4.16.

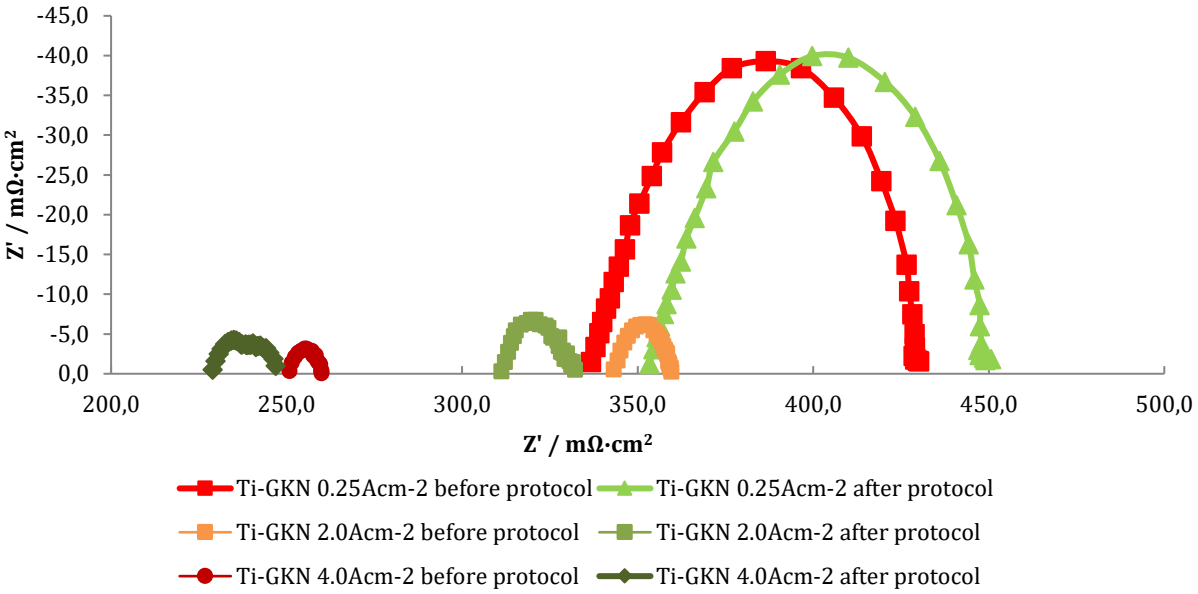

Figure 4.16 - Nyquist plots from the EIS measurements of Ti-GKN up to 4.0 A·cm^{-2} with a frequency range from 100 kHz to 50 mHz at 65 ºC before and after the FCR protocol.

The performance of Ti-GKN tends to improve by the end of the test. Even so, this change is not significant in the time interval of the tests. Furthermore, the corresponding ohmic losses decrease, noticeable by the slide of the EIS measurements to the left in the x-axis. The difference between the ohmic limitations determined previously and these values must be explained with future measurements, being that no MTL are registered.

It is also recommended that future protocols are carried out in automized systems which can maximize the electric connectivity of the system and minimize condensation of gases, with coated material, ventilations, rectifier, among other components that must react at a similar rate as the cell so that the results lead to exact conclusions.

Once again, Ti-GKN is proven to be a good PTL to satisfy boundaries and requirements from performance and response time, making this material a possible techno-economical and promising solution in this field that can easily react to any variations in the service grids.

5 Conclusion

Focused on the investigation of porous transport layers made of titanium, this work developed advanced characterization methodologies for the comparative study of PTLs with and without coating, with a special emphasis at the uncoated titanium and the Ti-GKN PTLs. All measurements aimed to be performed at 90 °C and up to 5.0 $A \cdot cm^{-2}$ hence economic efficiency.

In a study of a power variation in the performance of the cell, the compression pressure applied at the assembly was optimized at 1.0 N·m. This is the value with the highest efficiency and minimal overpotentials that decrease with the increase of the compression pressure. This behaviour switches, however, at high pressures, due to mechanical stress imposed at the structure. While for Ti mesh the stress is higher at certain compaction force due to its heterogeneous surface, the CCM applied to Ti-GKN pressures the material into the gaps of the mesh, providing a more homogeneous surface area.

The polarization curves showed a higher performance for Ti-GKN sample, with minimal mass transport limitations at higher current densities, opposed to other PTLs like Ti mesh, which shows that MTL prevent the PTLs from achieving cell performances whose values come close to the 2.70 V at 4.0 $A \cdot cm^{-2}$, value achieved with Ti-GKN. The coating applied to Ti-GKN successfully manages mass transport at higher current densities. The electrical limitations were responsible for the measured ohmic resistances, in result to conditions that were not found.

The EIS obtained confirmed the analysis of the polarization curves, confirming that a coated PTL is protected against corrosion and enables high catalytic activity characteristics such as improving mass transport losses (gas removal) at low and high current densities. The Ti-GKN PTL shows optimal electron and mass transport throughout the range of current densities, while the overpotentials generated at the uncoated PTL prevent an economical cell voltage.

Furthermore, simulations run in GeoDict confirmed the correlation between the structure of the coated PTLs with its performance and MTL. In fact, the path enhancement and lower tortuosity factor are characterized with lower overpotentials. The capillary pressure of Ti-GKN at 10 % saturation is 10 kPa. Its morphology allows a good gas removal so that no gas cushion is formed. In this way, the material reaches a faster state of saturation (all active centers are occupied with water flow), and consequently reaches a high performance.

In addition, the performed testing protocol for PEM electrolysers established the ability of Ti-GKN to satisfy the requirements of cell performance and response time, making this material a future standardized PTL for PEM in FCR service grids. Even so, the characterization

performed at this cell leaves unclear results on which further testing should analysed, recurring to larger automized systems with the same materials.

In conclusion, the higher contact area, porosity and larger pore radius, as well as the small thickness of the graded structure of the Ti-GKN enables this PTL to achieve the best cell performance and attract further studies that might confirm that this is very likely to become a standard material in H_2 production by the PEM electrolysis technology. In combination to other studies, the performances achieved at DLR have increase the cell performance with PTLs with a MPL and can lead to further developments regarding optimization of the layers on top of cheap meshes.

6 Assessment of the work done

6.1 Objectives Achieved

The research described in this paper contributes to a deeper understanding of the cell performance with coated PTLs at elevated temperatures and current densities through electrochemical characterization. The analysis of ICR measurements, polarizations curves and EIS measurements supports major contributors that lead to operational costs reduction and the decrease of the real potential and any changes concerning the operating conditions with current densities higher than 2.0 $A \cdot cm^{-2}$. In addition, properties simulated confirmed un-going studies of physical characterization of designed PTLs and the compression pressure for the assemblies was successfully optimized.

Even though it was not possible to characterize a ProH+ cell in operating conditions, a carried-out protocol confirmed the advantages of Ti-GKN for grid services under current densities up to 4.0 $A \cdot cm^{-2}$.

This paper demonstrates results that ergo economic efficiency of titanium PTLs at elevated temperatures and current densities.

6.2 Final Assessment

This work endures further studies of coated PTLs as future standard materials. Despite of the overall results, the time limitations along the semester imposed by the social environment around Europe intercepted the chance of carrying all desirable characterizations. In addition, technical difficulties in the test bench were an obstacle to run long-term tests and understand in an efficient matter the cell system.

In combat to the mentioned difficulties, it is recommended that in future work another test bench is used, and the opportunity to run tests in multiple cells simultaneously is offered. As noticed using the JCR protocols, the time interval set between measurements can also be a subject of change. Furthermore, higher performance values can be reached by combating the electrical limitations registered in this study. This can be done by preventing condensation and improving the connectivity of the materials, such is the case of the pins (not coated) and cables for the equipment.

The conclusion of the research project abroad is a milestone in my student life, applying skills developed throughout my career. The personal result is a visible growth on the ability to implement what I've learnt at FEUP and enhance career opportunities. Through a research

introspective, it's rewarding to feel that this work can lead to scientific improvements and contribute to the grow of knowledge at DLR in the topic of PEM electrolyzers.

7 References

[1] M. Carmo, D. L. Fritz, J. Mergel and D. Stolten, *A comprehensive review on PEM water electrolysis, International Journal of Hydrogen Energy*, no. 38, pp. 4901–4934, 2013.

[2] United Nations Framework Convention on Climate Change, 2020. (https://unfccc.int/)

[3] *Recent trends and projections in EU greenhouse gas emissions*, European Environment Agency, 2020. (https://www.eea.europa.eu/themes/climate/approximated-greenhouse-gas-emissions/approximated-greenhouse-gas-emissions-in-2017)

[4] *EU energy in figures 2019*, EU Publications, 2019, ISSN 978-92-76-08818-9.

[5] *Greenhouse Gas Inventory Data - Comparison by Category*, United Nations Framework Convention on Climate Change, 2020. (https://di.unfccc.int/comparison_by_category)

[6] REN, Dados técnicos - Technical Data 2019.

[7] G. Maggio, A. Nicita, G. Squadrito, *How the hydrogen production from RES could change energy and fuel markets: A review of recent literature*, International Journal of Hydrogen Energy, Volume 44, Issue 23, 2019, Pages 11371-11384, ISSN 0360-3199, https://doi.org/10.1016/j.ijhydene.2019.03.121.

[8] A. Sternberg and A. Bardow, *Power-to-What? – Environmental assessment of energy storage systems*, Energy Environ. Sci., vol. 8, no. 2, pp. 389–400, 2015.

[9] Richa Kothari, D. Buddhi, R.L. Sawhney, *Comparison of environmental and economic aspects of various hydrogen production methods*, Renewable and Sustainable Energy Reviews, Volume 12, Issue 2, 2008, Pages 553-563, ISSN 1364-0321, https://doi.org/10.1016/j.rser.2006.07.012.

[10] Yuansheng Huang, Shijian Liu, *Efficiency evaluation of a sustainable hydrogen production scheme based on super efficiency SBM model*, Journal of Cleaner Production, Volume 256, 2020, 120447, ISSN 0959-6526, https://doi.org/10.1016/j.jclepro.2020.120447.

[11] A. Buttler and H. Spliethoff, *Current status of water electrolysis for energy storage, grid balancing and sector coupling via power-to-gas and power-to-liquids: A review*, *Renew. Sustain. Energy Rev.*, vol. 82, no. September, pp. 2440–2454, 2018.

[12] Canan Acar, Ibrahim Dincer, *Comparative assessment of hydrogen production methods from renewable and non-renewable sources*, *International Journal of Hydrogen Energy*, Volume 39, Issue 1, 2014, Pages 1-12, ISSN 0360-3199, https://doi.org/10.1016/j.ijhydene.2013.10.060.

[13] S. Bennoua, A. Le Duigou, M.-M. Quéméré, S. Dautremont, *Role of hydrogen in resolving electricity grid issues, International Journal of Hydrogen Energy*, Volume 40, Issue 23, 2015, Pages 7231-7245, ISSN 0360-3199, https://doi.org/10.1016/j.ijhydene.2015.03.137.

[14] L. Allidières, A. Brisse, P. Millet, S. Valentin, M. Zeller, *On the ability of pem water electrolysers to provide power grid services*, International Journal of Hydrogen Energy, Volume 44, Issue 20, 2019, Pages 9690-9700, ISSN 0360-3199, https://doi.org/10.1016/j.ijhydene.2018.11.186.

[15] L., A. Chan, D. Hart, F. Lehner, B. Madden, and E. Standen, *Study on development of water electrolysis in the EU*, Fuel Cells and hydrogen Joint Undertaking, Fuel Cells Hydrog. Jt. Undert., no. February, pp. 1–160, 2014.

[16] German Federal Ministry for Economic Affairs and Energy (BMWi), *PlanDelyKad study on large scale water electrolysis and hydrogen storage*, BMWi, p. 298, 2015.

[17] A. S. Gago et al., *Protective coatings on stainless steel bipolar plates for proton exchange membrane (PEM) electrolysers*, J. Power Sources, vol. 307, pp. 815–825, 2016.

[18] J. Mo, S. M. Steen, F. Y. Zhang, T. J. Toops, M. P. Brady, and J. B. Green, *Electrochemical investigation of stainless steel corrosion in a proton exchange membrane electrolyzer cell*, Int. J. Hydrogen Energy, vol. 40, no. 36, pp. 12506–12511, 2015.

[19] P. Lettenmeier et al., *Comprehensive investigation of novel pore-graded gas diffusion layers for high-performance and cost-effective proton exchange membrane electrolyzers*, Energy Environ. Sci., vol. 10, no. 12, pp. 2521–2533, 2017.

[20] E. E. Haque, *Study of two-phase flow pressure drop characteristics in Proton Exchange Membrane (PEM) fuel cell flow channels of different geometries*, 2016. (https://www.researchgate.net/figure/Schematic-Diagram-of-a-Proton-Exchange-Membrane-PEM-fuel-cell-showing-the-HOR-and_fig1_304091318)

[21] Ö. F. Selamet, F. Becerikli, M. D. Mat, and Y. Kaplan, *Development and testing of a highly efficient proton exchange membrane (PEM) electrolyzer stack*, Int. J. Hydrogen Energy, 2011.

[22] T. Riis, E. Hagen, and P. Vie, *Hydrogen Production R+D: Priorities and Gaps*, France, 2006.

[23] P. Lettenmeier et al., *Durable Membrane Electrode Assemblies for Proton Exchange Membrane Electrolyzer Systems Operating at High Current Densities*, Electrochim. Acta, 2016.

[24] W. G. C. Ryan O'hayre, Suk-Won Cha, *Fuel Cell Fundamentals*, 2016.

[25] X. Z. Yuan, C. Song, H. Wang, and Z. J., *Electrochemical Impedance Spectroscopy in PEM Fuel Cells: Fundamentals and Applications*, 2010.

[26] T. Smolinka, E. Ojong, and T. Lickert, *Fundamentals of PEM Water Electrolysis, in PEM Electrolysis for Hydrogen Production: Principles and Applications*, D. Bessarabov, H. Wang, H. Li, and N. Zhao, Eds. Taylor & Francis Group, 2016.

[27] C. Wang, *Bipolar Plates and Plate Materials*, in *PEM Electrolysis for Hydrogen Production: Principles and Applications*, D. Bessarabov, H. Wang, H. Li, and N. Zhao, Eds. Taylor & Francis Group, 2016.

[28] P. Lettenmeier, A. S. Gago, and A. K. Friedrich, *Protective Coatings for Low-Cost Bipolar Plates and Current Collectors of Proton Exchange Membrane Electrolyzers for Large Scale Energy Storage from Renewables*, New Technol. Prot. Coatings, pp. 69–86, 2017.

[29] P. Lettenmeier et al., *Low-cost and durable bipolar plates for proton exchange membrane electrolyzers*, Sci. Rep., vol. 7, no. March, pp. 1–12, 2017.

[30] P. Lettenmeier, R. Wang, R. Abouatallah, F. Burggraf, A. S. Gago, and K. A. Friedrich, *Coated Stainless Steel Bipolar Plates for Proton Exchange Membrane Electrolyzers*, J. Electrochem. Soc., vol. 163, no. 11, pp. F3119–F3124, 2016.

[31] N. Briguglio and V. Antonucci, *Overview of PEM Electrolysis for Hydrogen Production*, in *PEM Electrolysis for Hydrogen Production: Principles and Applications*, D. Bessarabov, H. Wang, H. Li, and N. Zhao, Eds. Taylor & Francis Group, 2016.

[32] M. Carmo, W. Luke, and D. Stolten, *Electrocatalysts for the Hydrogen Evolution Reaction*, in *PEM Electrolysis for Hydrogen Production: Principles and Applications*, D. Bessarabov, H. Wang, H. Li, and N. Zhao, Eds. Taylor & Francis Group, 2016.

[33] S. A. Grigoriev, P. Millet, S. A. Volobuev, and V. N. Fateev, *Optimization of porous current collectors for PEM water electrolysers*, Int. J. Hydrogen Energy, vol. 34, no. 11, pp. 4968–4973, 2009.

[34] H. Ito, *Current Collectors (GDLs) and Materials*, in *PEM Electrolysis for Hydrogen Production: Principles and Applications*, D. Bessarabov, H. Wang, H. Li, and N. Zhao, Eds. Taylor & Francis Group, 2016.

[35] FuelCellStore, *Titanium Screen Mesh Cloth*. (http://www.fuelcellstore.com/titanium-screen-mesh-cloth)

[36] Y. Zhang, M. D. Merrill, and B. E. Logan, *The use and optimization of stainless steel mesh cathodes in microbial electrolysis cells*, Int. J. Hydrogen Energy, vol. 35, no. 21, pp. 12020–12028, 2010.

[37] C. M. Hwang et al., *Influence of properties of gas diffusion layers on the performance of polymer electrolyte-based unitized reversible fuel cells*, Int. J. Hydrogen Energy, vol. 36, no. 2, pp. 1740–1753, 2011.

[38] P. Lettenmeier, S. Kolb, F. Burggraf, A. S. Gago, and K. A. Friedrich, *Towards developing a backing layer for proton exchange membrane electrolyzers*, J. Power Sources, vol. 311, pp. 153–158, 2016.

[39] Oerlikon Metco, *An Introduction to Thermal Spray*, 2016.

[40] F. Azarmi, *Vacuum plasma spraying*, Toronto, 2005.

[41] GKN Sinter Metals, *Komponenten für den Antriebsstrang*, 2019.

[42] *EU Harmonised Polarisation Curve Test Method for Low Temperature Water Electrolysis*, JCR Validates Methods, Reference Methods and Measurements Report, JCR, 2018.

[43] STUDY ON EARLY BUSINESS CASES FOR H2 IN ENERGY STORAGE AND MORE BROADLY POWER TO H2 APPLICATIONS, 2017.

[44] A. Nechache, M. Cassir, and A. Ringuedé, *Solid oxide electrolysis cell analysis by means of electrochemical impedance spectroscopy: A review*, J. Power Sources, vol. 258, pp. 164–181, 2014.

[45] C. Rozain and P. Millet, *Electrochemical characterization of Polymer Electrolyte Membrane Water Electrolysis Cells*, Electrochim. Acta, vol. 131, pp. 160–167, 2014.

[46] I. Dedigama et al., *In situ diagnostic techniques for characterisation of polymer electrolyte membrane water electrolysers e Flow visualisation and electrochemical impedance spectroscopy*, Int. J. Hydrogen Energy, vol. 39, no. 9, pp. 4468–4482, 2014.

[47] J. C. Garcia-navarro, M. Schulze, and K. A. Friedrich, *Measuring and modeling mass transport losses in proton exchange membrane water electrolyzers using electrochemical impedance spectroscopy*, J. Power Sources, vol. 431, no. December 2018, pp. 189–204, 2019.

[48] Metrohm, *Electrochemical Impedance Spectroscopy (EIS) Part 1 – Basic Principles*, 2011.

[49] T. Malkow, A. Pilenga and G. Tsotridis, *EU Harmonised test procedure: electrochemical impedance spectroscopy for water electrolysis cells*, JCR Validates Methods, Reference Methods and Measurements Report, JCR, 2018.

[50] GeoDict, *Solutions: The Digital Material Laboratory*, 2020. (https://www.math2market.com/Solutions/aboutGD.php)

[51] A. Wiegmann, E. Glatt, A. Griesse, M. Kabel, T. Schmidt and F. Schimmer, *Digital Twin – How to generate and validate modelled microstructures from 2D and 3D images*, Math2Market GmbH, 2018. (https://www.geodict.com/Presentations/2018MSE_1_CB.pdf)

[52] GeoDict, *The PoroDict module*, 2020. (https://www.math2market.com/Modules/Dicts/PoroDict.php)

[53] O. F. Selamet and M. S. Ergoktas, *Effects of bolt torque and contact resistance on the performance of the polymer electrolyte membrane electrolyzers*, J. Power Sources, vol. 281, pp. 103–113, 2015.

Appendice A – Polarization Curves of Ti-GKN and Ti mesh at Different Compression Pressures

This appendice offers the division of Figure 4.2 in Chapter 4 into two plots for a better visualization of the polarization curves of Ti-GKN (Figure A.1) and Ti mesh (Figure A.2) in the study of the effect of the compression pressure on the electrochemical characterization of these PTLs.

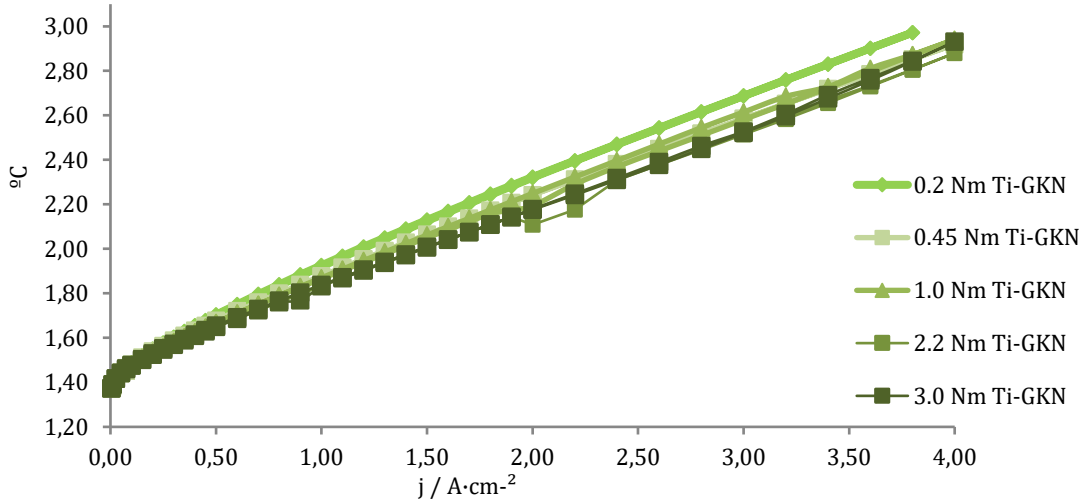

Figure A.1 - Polarization curves of Ti-GKN for multiple compression pressures up to 4.0 A·cm^{-2}.

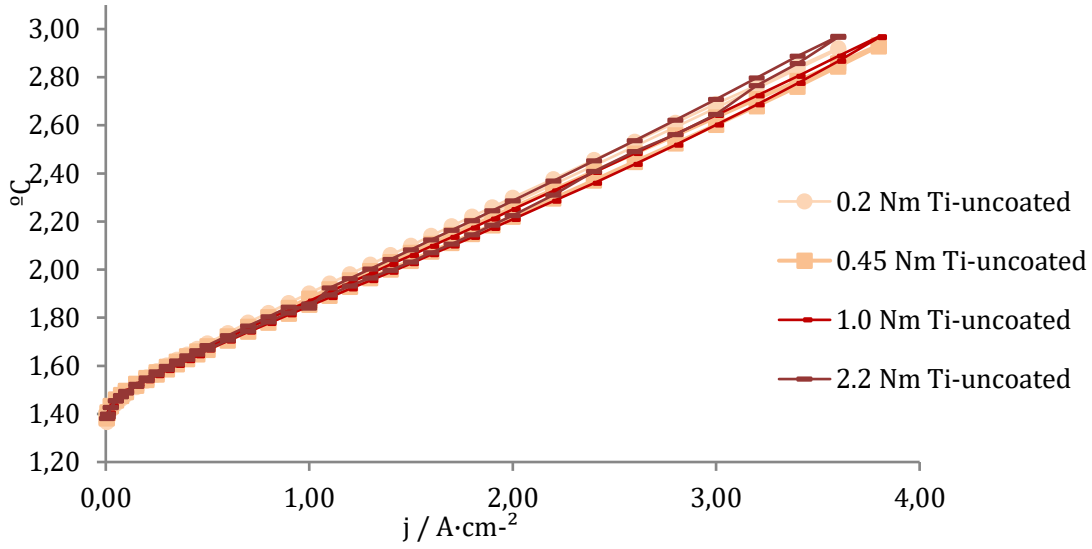

Figure A.2 - Polarization curves of Ti mesh for multiple compression pressures up to 4.0 A·cm^{-2}.

Appendice B – GeoDict Simulation Full Results

In response to the solver programmes described in Chapter 3, the full results of the bubble point and tortuosity factor are shown in Table B.1, while Figure B.1 presents the capillary pressure curves.

Table B.1 - Bubble point and tortuosity factor of the Ti-Ti/Nb, Ti-Ti and Ti-GKN PTLs.

	Ti-Ti/Nb	Ti-Ti	Ti-GKN
Bubble Point (Pa)	810.91	494.04	854.42
Tortuosity Factor	2.24	2.07	2.17

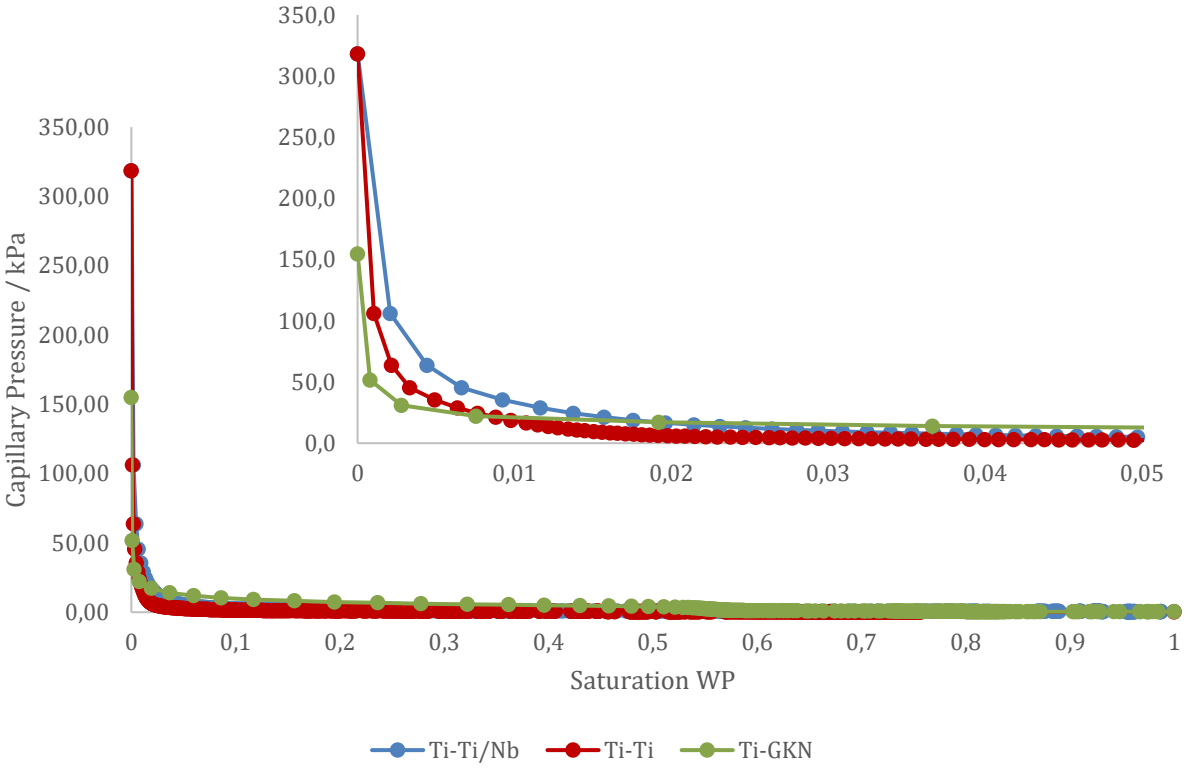

Figure B.1 - Capillary pressure curve of the Ti-Ti/Nb, Ti-Ti and Ti-GKN PTLs.